Ferroptotic vulnerability of post-meiotic germ cells skews sex chromosome ratios in aged testis

Jasper K. Germeraad[1], Takako Kikkawa[1]*, Junya Ito[2,3], Leon S.Y. Giesselink[4], Wilfred T.V. Germeraad[5], Bernhard Henkelmann[3], Maceler Aldrovandi[3], Kenshiro Hara[6], Kentaro Tanemura[6], Kiyotaka Nakagawa[2], Eikan Mishima[3,7], Marcus Conrad[3,8], Noriko Osumi[1]*

[1]Department of Developmental Neuroscience, Tohoku University Graduate School of Medicine, Sendai, Japan

[2]Laboratory of Food Function Analysis, Graduate School of Agricultural Science, Tohoku University, Sendai, Japan

[3]Institute of Metabolism and Cell Death, Molecular Targets and Therapeutics Center, Helmholtz Munich, Neuherberg, Germany

[4]Centre for Health Protection, National Institute for Public Health and the Environment (RIVM), Bilthoven, The Netherlands

[5]Department of Internal Medicine, Division of Haematology, Maastricht University Medical Center, Maastricht, The Netherlands

[6]Laboratory of Animal Reproduction and Development, Graduate School of Agricultural Science, Tohoku University, Sendai, Japan

[7]Environmental Medicine and Molecular Toxicology, Graduate School of Medicine, Tohoku University, Sendai, Japan

[8]Translational Redox Biology, Natural School of Sciences, Technical University of Munich, Garching, Germany

Running title: Non-apoptotic cell death in aged testes

Keywords**:** Spermatogenesis, regulated cell death, lipid peroxidation, vitamin E

*Corresponding author
Noriko Osumi, PhD
Professor, Department of Developmental Neuroscience,
Tohoku University Graduate School of Medicine,
2-1 Seiryo-machi, Aoba-ku, Sendai 980-8575, Japan
Tel.: +81 22 717 8201. Fax: +81 22 717 8205.
E-mail address: noriko.osumi.c7@tohoku.ac.jp (N. Osumi)

Takako Kikkawa, PhD
Assistant Professor, Department of Developmental Neuroscience,
Tohoku University Graduate School of Medicine,
2-1 Seiryo-machi, Aoba-ku, Sendai 980-8575, Japan
Tel.: +81 22 717 8203. Fax: +81 22 717 8205.
E-mail address: takako.kikkawa.c4@tohoku.ac.jp (T. Kikkawa)

Grant Sponsors: JSPS KAKENHI (#17K19372, 22K19322, 25K22536), The Canon Foundation, JST FOREST Program (JPMJFR2213), European Union's Horizon 2020 research and innovation program (GA 884754).

Abstract

Age-related testicular germ cell depletion has been predominantly attributed to apoptosis; however, the contribution of alternative cell death modalities remains unclear. Using young and aged mice, we demonstrate compartment-specific cell-death signatures in the testis. Apoptotic cell increased in peripheral germ layers, whereas the luminal round spermatid (RS) layer mainly accumulated non-apoptotic events sharing features with ferroptosis, a lipid-peroxidation dependent cell death. Lipidomic analysis revealed age-related phospholipid remodelling in whole testis, while RS-enriched fractions showed increased lipid peroxidation. Interestingly, aging shifted the balance of sex-chromosome–bearing RS toward Y-bearing cells, and this bias persisted in mature sperm. Dietary vitamin E modulated these phenotypes bidirectionally: vitamin E deficiency in young mice increased RS lipid peroxidation and reproduced the Y-skew, whereas supplementation in aged mice lowered RS lipid peroxidation, decreased non-apoptotic events, and restored the skewed RS sex-chromosome ratio. These findings define an age-related RS vulnerability linking redox stress to haploid spermatogenic output.

61 **Introduction**

62 Advanced paternal age is associated with reduced semen volume, lower sperm concentration
63 and motility, and increased sperm DNA fragmentation[1–3]. Although male fertility can be
64 maintained throughout life, reproductive capacity progressively declines because of age-
65 dependent deterioration of testicular function[4]. Sperm are produced through spermatogenesis,
66 a strictly controlled process within the seminiferous tubules in which spermatogonial stem cells
67 generate differentiating spermatogonia, meiotic spermatocytes and post-meiotic haploid round
68 spermatids (RSs) that subsequently elongate into spermatozoa[5]. Each round spermatid (RS)
69 carries either a Y- or an X-chromosome. Therefore, selective survival or loss at post meiotic
70 stages has the potential to bias sex-chromosome transmission by altering the relative
71 representation of Y- and X-bearing gametes. While age-related impairment of murine
72 spermatogenesis is well documented[6–8], the mechanisms driving germ-cell loss during
73 testicular aging remain insufficiently understood, particularly at post-meiotic stages[9].
74
75 Germ-cell loss in aging testes has frequently been linked to oxidative stress-induced
76 apoptosis[10,11]. However, oxidative stress can activate multiple cell death modalities[12], and
77 susceptibility is likely to vary along the germ-cell differentiation axis. Previous reports showed
78 that pre-meiotic germ and somatic cells predominantly engage apoptosis[13], whereas recent *in*
79 *vitro* studies suggests that spermatocytes and RSs respond differently to oxidative insults,
80 including lipid peroxides[14]. RS membranes are enriched in polyunsaturated phospholipids and
81 undergo extensive membrane remodelling, features predicted to increase sensitivity to lipid
82 peroxidation[15,16]. Consistent with this notion, elevated lipid peroxidation represents a recurring
83 biochemical signature of reproductive aging in testes[17].
84
85 Lipid peroxidation can trigger ferroptosis, a non-apoptotic form of cell death driven by iron-
86 mediated phospholipid peroxidation[18]. Ferroptosis susceptibility is shaped by three core pillars:
87 antioxidant defence mechanisms, membrane phospholipid composition and control of labile
88 iron[19,20]. For instance, the selenoenzyme glutathione peroxidase 4 (GPX4) detoxifies
89 potentially harmful lipid hydroperoxides, and impaired GPX4 functions confers cellular
90 vulnerability to ferroptosis[21,22]. Conversely, long-chain fatty acid CoA ligase 4 (ACSL4)
91 promotes incorporation of poly-unsaturated fatty acids (PUFAs) into membrane phospholipids,
92 generating highly peroxidizable substrates that sensitize cells to ferroptosis[23]. Iron-handling
93 pathways further modify this process; transferrin receptor 1 (TFR1) mediated iron uptake and

heme oxygenase-1 (HO-1) dependent heme degradation can elevate iron levels, amplifying ferroptotic sensitivity[24].

Ferroptosis is suppressed by lipophilic antioxidants, among which vitamin E is one of the most potent natural antioxidants that limits membrane lipid peroxidation and exerts anti-ferroptotic activity[25]. Vitamin E deficiency induces spermatogenic defects resembling features of reproductive aging[26] and can preferentially reduce post meiotic germ-cell populations, despite differences in dietary regimens and species[27]. These observations suggest that disruption of lipid redox homeostasis may be sufficient to activate aging-relevant vulnerability pathways, with RSs representing a particularly susceptible stage where lipid peroxidation could selectively influence the survival of X- versus Y-bearing haploid cells.

Here, we investigate how aging alters spermatogenic output and cell death modalities, including apoptosis and ferroptosis, across the seminiferous epithelium. We characterize age-related lipid peroxidation and related defence pathways in whole testis and in RS-enriched fractions and quantify sex-chromosome ratios in both RSs and mature sperm. Additionally, by bidirectionally manipulating dietary vitamin E, through deficiency in young mice and supplementation in aged mice, we test whether aging-associated RS vulnerability and sex-chromosome ratio shifts are causally linked to the dysregulation of the lipid peroxidation-ferroptosis axis.

115 **Results**

116 **Aging impairs spermatogenesis and promotes non-apoptotic cell death in RSs**

117 By 18 months of age, C57BL/6J males exhibit measurable testicular aging[28]. To investigate
118 aging-related gonadal changes, we therefore compared young (3-month-old) and aged (18-
119 month-old) male mice. Aged mice displayed increased body weight (Fig. 1a) and decreased
120 testis weight (Fig. 1b), resulting in a lower gonadosomatic index (testis weight/body weight,
121 Fig. 1c). To assess spermatogenic output in aged mice, we focused on stage VII-VIII
122 seminiferous tubules, which contain undifferentiated spermatogonia, differentiating
123 spermatogonia, meiotic pachytene spermatocytes, post-meiotic RSs and somatic Sertoli cells
124 (spermatogenesis support cells), thus representing key stages of spermatogenesis (Fig. 1d).
125 Testis from aged mice showed reduced cellular density in germ and somatic cells of the
126 seminiferous epithelium (Fig. 1e). Quantitative analysis showed a reduction in undifferentiated
127 spermatogonia in aged compared with young testes (Fig. 1f), which extended to differentiating
128 spermatogonia, pachytene spermatocytes, RSs, and was also observed in somatic SCs (Fig. 1g–
129 j).

130

131 Next, to investigate germ cell type–specific cell death associated with aging, we evaluated cell
132 death using terminal deoxynucleotidyl transferase dUTP nick end labelling (TUNEL) across
133 seminiferous tubules, irrespective of stage. Although TUNEL staining was classically used as
134 a marker of apoptosis, it is also known to detect cells undergoing other regulated cell death
135 modalities[19]. A higher proportion of seminiferous tubules in aged mice contained TUNEL-
136 positive dead cells compared to those in young mice (Extended data Fig. 1a, b).

137

138 To identify apoptotic cells, we performed double labelling with TUNEL (a general cell death
139 marker) and immunostaining against cleaved-caspase3 (CASP3), a specific marker of
140 apoptosis. We quantified $CASP3^{+}/TUNEL^{+}$ cells (apoptotic) and $CASP3^{-}/TUNEL^{+}$ cells (dead
141 cells) separately within the peripheral compartment, containing spermatogonia, spermatocytes
142 and Sertoli cells, and the luminal layer, which is enriched in RSs (Fig. 1k). In the peripheral
143 compartment, aging mice showed a significantly larger number of $CASP3^{+}/TUNEL^{+}$ apoptotic
144 cells (Fig. 1l), whereas the number of $CASP3^{-}/TUNEL^{+}$ dead cells remained unchanged (Fig.
145 1m). In contrast, within the luminal layer, $CASP3^{+}/TUNEL^{+}$ apoptotic RSs were rare and did
146 not differ between age groups (Fig. 1n, Extended Data Fig. 1c), while $CASP3^{-}/TUNEL^{+}$ cells
147 prevailed and were more abundant in aged testes (Fig. 1o). Although cleaved CASP3 can be
148 transient, the marked enrichment of $CASP3^{-}/TUNEL^{+}$ events specifically in the luminal RS

149 layer supports a compartment-specific shift toward TUNEL^{+} cell-death events without
150 detectable CASP3 activation in aging testes.
151
152 **Aging enhances lipid peroxidation in RSs**
153 Increased lipid peroxidation is a feature of testicular aging and capable of inducing cell death
154 in aging rodent models[29–31]. To define age-related changes in phospholipid composition and
155 oxidation status, we profiled testicular phospholipids by mass-spectrometry-based lipidomic
156 analysis. Consistent with previous studies[32,33], phosphatidylcholine (PC) and
157 phosphatidylethanolamine (PE) constituted the predominant phospholipid classes detected in
158 mouse testis (Extended Data Fig. 2a, b). Age-related changes in individual PC and PE species
159 were modest overall, although aged testes showed an increase in PC plasmalogen species
160 (Extended Data Fig. 2c), but not PE plasmalogen species (Extended Data Fig. 2d). The increase
161 in PC plasmalogen species may reflect age-dependent remodelling of ether lipids, which are
162 implicated in antioxidant defence under oxidative stress conditions[34].
163
164 Given that RSs are enriched in polyunsaturated phospholipid species[15], this may suggest
165 heightened vulnerability to oxidative stress and lipid peroxidation. We isolated RS-enriched
166 fractions from young and aged testes using a density-gradient (Fig. 2a) and confirmed >80%
167 RS purity by peanut agglutinin (PNA) staining and nuclear morphology (Extended Data Fig.
168 3). Immunoblot analysis of RS-enriched fractions revealed increased levels of 4-
169 hydroxynonenal (4HNE)-modified proteins in aged compared with young samples, indicating
170 enhanced lipid peroxidation in aged RSs (Fig. 2b). In line, gene expression levels of *Alox15*,
171 encoding a PUFA-oxidizing lipoxygenase, was elevated in aged RSs (Fig. 2c). Because
172 susceptibility to lipid peroxidation is influenced by how PUFAs are incorporated into
173 membrane phospholipids[23], we examined gene expression levels of key enzymes involving
174 PUFA loading and elongation. In aged RSs, expression of *Acsl4,* encoding an acyl-CoA
175 synthetase that facilitates arachidonic/adrenic acid (AA/AdA)-PUFA enrichment in
176 phospholipids, was increased, whereas other ACSL family genes such as *Acsl6* and the PUFA-
177 elongating enzymes *Elovl2* and *Elovl5* were not altered with age (Fig. 2d, e, Extended Data Fig.
178 2e, f). Together, these data are consistent with a selective shift toward AA/AdA-type PUFA
179 phospholipid remodelling rather than enhanced docosahexaenoic acid (DHA) loading in aged
180 RSs, supporting increased susceptibility of AA/AdA-containing phospholipids to oxidation.
181
182 **Aging reduces cGpx4 expression and remodels iron handling in RSs**

183 To investigate the mechanism underlying increased lipid peroxidation in aged testes, we
184 assessed antioxidant defence and iron-handling pathways in RSs. GPX4 is a central regulator
185 of lipid peroxide detoxification and the prime regulator of ferroptosis. Immunostaining
186 confirmed GPX4 expression in the RS cytoplasm and in the sperm tail (Extended Data Fig. 4a).
187 In testis, GPX4 is expressed as three isoforms: nuclear (nGPX4), mitochondrial (mGPX4) and
188 cytosolic (cGPX4) isoforms, of which cGPX4 has been implicated as the critical isoform
189 protecting germ cell from cell death[35–38]. We therefore quantified *Gpx4* mRNA transcripts in
190 RSs from young and aged mice, using primer sets targeting the nuclear (*nGpx4*) transcript and
191 the mitochondrial-targeted (*mGpx4*) transcript, together with a primer set amplifying both
192 mitochondrial and cytosolic (*cGpx4*) transcripts[39]. Using this strategy, we estimated the *cGpx4*
193 fraction as the difference between the shared signal and the mitochondrial-specific signal.
194 While *nGpx4* and *mGpx4* were unchanged with age, *cGpx4* expression was reduced in aged
195 RSs (Fig. 2f–h). Total GPX4 protein levels, detected with an antibody recognizing all isoforms,
196 did not differ between young and aged RSs fractions (Fig. 2i). Given the predominance of
197 mGPX4 in RSs[36], these findings suggest that age-associated downregulation of *cGpx4* occurs
198 without a detectable change in bulk RS GPX4 protein levels.
199
200 Nuclear erythroid factor 2 (NRF2) controls a broad antioxidant and cytoprotective program[40]
201 (Fig. 2j). Among NRF2 target genes, superoxide dismutase-*1* (*Sod1*) and catalase (*Cat*)
202 mRNAs did not change in RSs (Fig. 2k–m), whereas *HO-1* was selectively induced in aged
203 RSs (Fig. 2n), consistent with increased heme catabolism. Because HO-1 can elevate the labile
204 iron pool, we assessed iron handling and found increased *Tfr1* mRNA and increased ferritin
205 heavy chain (FTH1), with no change in ferritin light chain (FTL) and nuclear receptor co-
206 activator 4 (NCOA4) protein in aged RSs (Fig. 2o–s; Extended Data Fig. 4b, c). Together, these
207 changes support an age-associated shift toward a more pro-oxidant iron environment in RSs
208 (Fig. 2t), which would be expected to sensitize these cells to iron-dependent lipid damage.
209
210 **Aging skews the Y/X sex chromosome ratio in RSs and mature sperm**
211 Since *Acsl4* is encoded by the X-chromosome and is upregulated in aged RSs (Fig. 2f), we
212 asked whether aging is associated with a bias in the relative abundance of X- and Y-bearing
213 RSs. To distinguish X- and Y-bearing RSs, we performed fluorescent *in situ* hybridization
214 (FISH), targeting the X- and Y- chromosome with specific probes. We found that the ~1:1 ratio
215 was maintained in young testes but was significantly skewed toward Y-bearing RSs in aged
216 testes (young: mean Y/X ratio 1.02 [n = 6,282±100 Y-RSs, n = 6,188±113 X-RSs]; aged: mean

217 Y/X ratio 1.11 [n = 6,694±85 Y-RSs, n = 6,056±98 X-RSs]; Fig. 3a,b). To determine whether
218 this bias persisted in mature sperm, we quantified X- and Y-bearing sperm using fluorescent
219 activated cell sorting (FACS) using Hoechst-33342 to visualize the DNA content difference
220 between Y- and X- bearing RSs (Fig. 3c, d). Consistent with the findings in RSs, the Y/X ratio
221 was similarly shifted toward Y-bearing sperm in aged males compared with young controls
222 (young: mean Y/X 1.02 [n = 3,382,147 ± 140,662 Y-sperm vs n = 3,293,224 ± 126,522 X-
223 sperm]; aged: mean Y/X 1.09 [n = 3,294,779 ± 156,878 Y-sperm; n = 3,032,412 ± 145,748 X-
224 sperm], Fig. 3e,f). These results indicate that aging is associated with a bias toward Y-bearing
225 RSs, and this sex chromosome bias is maintained in mature sperm.
226
227 **Vitamin E depleted diet recapitulated aging-associated phenotypes**
228 Given the elevated lipid peroxidation observed in aged testis, we asked whether a lipid
229 peroxidation-prone condition induced by vitamin E-depleted diet may cause aging-like
230 testicular phenotypes in young mice[26]. Young animals were fed either a vitamin E-deficient
231 diet (VE(−), <0.1mg/kg vitamin E) or control diet (135mg/kg vitamin E) for two cycles of
232 spermatogenesis[5] (70 days, Fig. 4a). Although body weight, testis weight and gonadosomatic
233 index were not affected by vitamin E-deficient diet (Fig. 4b–d), VE(−) testes showed impaired
234 spermatogenic output (Fig. 4e). Quantitative analysis revealed that numbers of undifferentiated
235 and differentiating spermatogonia remained unchanged, whereas pachytene spermatocytes,
236 RSs and Sertoli cells were reduced in VE(−) testes compared with controls (Fig. 4f–j),
237 indicating impaired spermatogenic progression.
238
239 Consistent with the reduction in germ and somatic cell numbers, VE(−) testes contained more
240 TUNEL$^+$ dead cells than control testes (Extended Data Fig. 5a, b). When cell death was
241 analysed separately in the peripheral compartment and the luminal RS layer (Fig. 4k), vitamin
242 E deficiency significantly increased CASP3$^+$/TUNEL$^+$ apoptotic cells in the peripheral regions
243 without altering CASP3$^-$/TUNEL$^+$ cells (Fig. 4k, l). By contrast, in the luminal compartment,
244 vitamin E-deficient diet only induced a trend toward higher CASP3$^-$/TUNEL$^+$ non-apoptotic
245 RSs, but CASP3$^+$/TUNEL$^+$ RSs remained rare and unchanged (Fig. 4l, m; Extended Data Fig.
246 5d). Together, vitamin E deficiency preferentially elevates apoptosis-associated death events
247 in the peripheral compartment, while its effect on RS-layer CASP3$^-$/TUNEL$^+$ events is weaker
248 under these conditions.
249

250 In RSs isolated from VE(−) testes, expression of lipid-metabolic and stress-response genes was
251 significantly altered. *Acsl4, Hmox1, Ftl* and *Tfr1* transcripts were upregulated, whereas all three
252 *Gpx4* isoforms were reduced (Fig. 4n). Consistent with enhanced lipid peroxidation, the levels
253 of 4HNE-modified proteins were elevated in VE(−) RSs (Fig. 4o). At the protein level, FTH1
254 was decreased, whereas total GPX4, FTL and NCOA4 were unaffected (Fig. 4p-t).
255
256 We further examined whether feeding mice with a vitamin E-deficient diet altered the sex
257 chromosome composition of RSs. In control testes, Y- and X-bearing RSs were similar in
258 number, whereas VE(−) testes exhibited a significant enrichment of Y-bearing RSs (control:
259 mean Y/X ratio 1.02 [n = 6,390±125 Y-RSs vs n = 6,274±127], X-RSs; VE(−): Y/X ratio 1.07
260 [n = 6,548±222 Y-RSs vs n = 6,186±212 X-RSs]; Fig. 4u). Overall, vitamin E deficiency in
261 young mice induced an aging-like RS stress state, with increased lipid peroxidation and broad
262 remodelling of lipid/iron-defence transcripts in RS fractions. Notably, despite limited induction
263 of RS-layer $CASP3^{-}/TUNEL^{+}$ events, vitamin E deficiency produced a significant shift in
264 haploid output, enriching Y-bearing RSs, thereby recapitulating the sex-chromosome skew
265 observed in aged testes.
266
267 **Vitamin E supplementation reduced aging-associated testicular phenotypes**
268 Given that vitamin E deficiency in young mice recapitulated multiple aging-like testicular
269 phenotypes, we next asked whether vitamin E supplementation could counteract these changes
270 in aged mice. To this end, aged animals were fed either a vitamin E-supplemented diet (VE(+))
271 or control diet according to the regimen shown in Fig. 5a. Body weight, testis weight and
272 gonadosomatic index did not differ between VE(+) and control groups (Fig. 5a–d), indicating
273 that vitamin E supplementation does not affect gross somatic growth or testis size in aged mice
274 during this feeding regimen. Despite unchanged testis size, VE(+) improved spermatogenic
275 output in aged mice (Fig. 5e). While the numbers of undifferentiated and differentiating
276 spermatogonia were not altered, pachytene spermatocyte, RS and Sertoli cell numbers were
277 significantly increased in VE(+) compared with control testes (Fig. 5f–j). Consistent with this
278 improvement, VE(+) testes contained fewer $TUNEL^{+}$ cells than control testes (Extended Data
279 Fig. 5a, c). In the peripheral compartment, vitamin E supplementation significantly lowered
280 the $Casp3^{+}/TUNEL^{+}$ apoptotic population without affecting $CASP3^{-}/TUNEL^{+}$ cells (Fig. 5k,
281 l). In contrast, within the luminal RS layer, VE(+) selectively reduced non-apoptotic
282 $CASP3^{-}/TUNEL^{+}$ RSs, whereas $CASP3^{+}/TUNEL^{+}$ apoptotic RSs remained infrequent and
283 unchanged across groups (Fig. 5k, m, Extended Data Fig. 5d). These results indicate that

284 vitamin E attenuates apoptosis in the periphery and CASP3^{-}/TUNEL^{+} non-apoptotic events in
285 the luminal layer, consistent with reduced oxidative burden.
286
287 We next assessed the transcriptional changes in RSs from aged mice. In VE(+) RSs, *Alox15*
288 mRNA was significantly reduced, whereas expression of other lipid/oxidized lipid-metabolic
289 genes including, *Gpx4*, NRF2-target genes and iron-related transcripts were unchanged relative
290 to the aged controls (Fig. 5n). Nonetheless, 4HNE-modified protein levels were significantly
291 reduced in VE(+) RSs (Fig. 5o). Among iron-handling proteins, in RSs from VE(+) mice,
292 FTH1 and FTL protein levels were significantly reduced, whereas NCOA4 was increased (Fig.
293 5q–t), a pattern consistent with enhanced ferritin turnover, suggesting mobilization of ferritin-
294 bound iron; however, whether this increases the labile iron pool or is coupled to iron
295 utilization/export remains to be determined.
296
297 VE(+) also exerted an opposite effect on the RS sex chromosome composition compared to
298 VE(−). In aged control testes, Y-bearing RSs outnumbered X-bearing RSs, whereas, in contrast,
299 VE(+) restored the Y- and X-bearing RSs ratio to a near 1:1 ratio (control: mean Y/X ratio 1.10
300 [n = 6,527±135 Y-RSs vs n = 5,950±156 X-RSs]; VE(+): Y/X ratio 1.01 [n = 5,772±156 Y-
301 RSs vs n = 5,702±149 X-RSs]; Fig. 5u). Taken together, the vitamin E deficiency and
302 supplementation experiments show that in vitamin E deficient conditions, higher lipid
303 peroxidation is associated with enrichment of Y-bearing RSs, whereas vitamin E
304 supplementation in aged mice lowers lipid peroxidation and restores the RS sex ratio toward
305 ~1:1. These findings are consistent with preferential vulnerability of X-bearing RSs under
306 conditions of elevated lipid peroxidation.
307

308 **Discussion**

309 Aging in mammals is accompanied by testicular atrophy and progressive decline in
310 spermatogenic capacity[28,41,42]. Here, we identified post-meiotic RSs as a particularly age-
311 sensitive stage in which lipid peroxidation increases, coinciding with a compartment-specific
312 shift in death signatures and an altered haploid sex-chromosome output. Dietary modulation of
313 vitamin E reversed these phenotypes, indicating that membrane redox buffering can influence
314 spermatogenic efficiency and the relative abundance of Y- and X-bearing haploid cells.
315
316 Aging increased germ-cell death, but not uniformly across the seminiferous epithelium.
317 Peripheral layers showed an apoptotic signature consistent with prior work [43,44], whereas the
318 luminal RS layer accumulated predominantly non-apoptotic TUNEL^{+} events. This stage
319 specificity may reflect intrinsic vulnerabilities of RSs, whose membranes are enriched in
320 peroxidation-prone PUFAs[15,45], potentially pushing RSs closer to a lipid-damage threshold.
321 RS-enriched fractions indeed displayed characteristics indicative of enhanced lipid
322 peroxidation and reduced antioxidant capacity. The convergence of lipidomic oxidation
323 signatures, altered antioxidant and iron-handling pathways, and bidirectional modulation by
324 vitamin E supports a death modality that shares features with ferroptosis[18,23,46].
325
326 A striking consequence of this RS vulnerability is a shift in haploid sex-chromosome
327 composition. We observed a skew toward Y-bearing RSs in aged testes, indicating that the sex-
328 chromosome ratio can deviate from ~1:1 and persists in mature sperm. Because the skew is
329 already present at the RS stage, it is unlikely to arise solely from selective processes during
330 epididymal transit, although upstream meiotic drive and downstream quality-control
331 mechanisms could still change the final output[47,48]. Round spermatids share gene transcripts
332 across cytoplasmic bridges[49], however, incomplete sharing of gene products across
333 intercellular bridges provides a plausible route for divergence between X- and Y-bearing RSs,
334 and geno-informativity analyses have identified incompletely shared gene transcripts relevant
335 to lipid peroxidation pathways[50]. Interestingly, independent *in vitro* studies report an X-skew
336 among surviving mature sperm following acute oxidative stress[51]. Although the direction of
337 this bias differs from our observed RS-stage Y-skew, the two observations are not directly
338 comparable given differences in developmental stage, context, and stress regime. Nonetheless,
339 our dietary vitamin E data indicate that membrane redox buffering can influence RS haploid
340 output, shifting the Y/X ratio toward or away from parity, consistent with the broader principle

that redox conditions can bias sex-chromosome representation at the gamete level[52], potentially via differential vulnerability of X- and Y-bearing cells.

This study has several limitations. First, although the lipid peroxidation profile and vitamin E sensitivity in RSs support a lipid damage state, definitive pathway assignment *in vivo* is constrained by the essential role of GPX4 in spermatogenesis, which limits straightforward genetic testing of this axis. Establishing causality will therefore require complementary approaches, such as perturbation of more genetically tractable suppressor pathways. Second, the basis of the aging-associated Y/X skew remains unknown because RS-enriched fractions were not sex-resolved and upstream or downstream selection may also contribute. Finally, we did not test whether vitamin E modifies the Y/X ratio in offspring sex ratio in aged males, which will require controlled mating studies.

Overall, our findings position RSs as a key stage at which aging-associated lipid redox stress may bias haploid sex-chromosome ratios (Extended Data Fig. 6). Defining how lipid peroxidation, antioxidant capacity and Y- versus X-linked vulnerabilities are coordinated *in vivo* will be important for understanding how male reproductive aging shapes sex-chromosome transmission.

Methods

Animals

Male C57BL/6J mice were maintained in the Animal Experiment Facility at the Tohoku University Graduate School of Medicine. All animals were housed in standard cages in a temperature- and humidity-controlled room on a 12-hour light/dark cycle (light on at 8 am) and had access to food and water ad libitum. All experimental procedures were approved by the Ethics Committee for Animal Experiments in Tohoku University (#2023-MED03701), and the animals were treated according to the National Institutes of Health (NIH) guide for the care and use of laboratory animals. For age-comparison experiments, C57BL/6J mice were obtained from Charles River Laboratories and were bred and maintained in-house. Mice were sacrificed at 3 months old (Young) or 18 months old (Aged).

Vitamin E feeding

A separate cohort of male 1-month and 16-month-old C57BL/6J mice was purchased from Jackson Laboratories (JAX, Japan). Vitamin E diets were custom-made and ordered from Funabashi Farm, Japan. 1-month-old animals were fed control (containing 135 mg/kg vitamin E) or vitamin E-deficient diet (VE(−), containing <0.1 mg/kg vitamin E), and 16-month-old animals were maintained on control or vitamin E-supplemented diet (VE(+), containing 500 mg/kg vitamin E). Detailed ingredients are listed in Extended Data Table 1. All mice were raised on these diets for 10 weeks (70 days), covering two full cycles of spermatogenesis (35 days)[7], after which mice were sacrificed at 3- and 18-months of age, respectively.

Testis collection

Animals were sacrificed by sedation with isoflurane (MSD Animal health) and cervical dislocation. Testes were isolated, separated from the surrounding fat tissue and epididymis and weighed together. Samples were then fixed in 4% paraformaldehyde in phosphate buffered saline (PBS, 4% PFA, Nacalai-Tesque) for 2 hours at 4°C, cut in half, and fixed for an additional 18 hours. Cryoprotection was executed as follows: the testes samples were immersed, sequentially, in 10% sucrose dissolved in PBS for 1 hour and 20% sucrose in PBS overnight, both at 4˚C. After cryoprotection, samples were frozen in Tissue-Tek optimal cutting compound (OCT, Sakura Finetek) on a metal pedestal using liquid nitrogen and stored in -80°C until further use. Cryosections (10µm) were obtained using a cryostat (Leica CM3050 S) and used for histological analyses.

393 **Immunohistochemistry (IHC)**

394 Testicular sections on slide glasses (Matsunami) were stained using a previously established
395 method[53] with antibodies targeting anti-PLZF (1:500, sc28319, Santa Cruz), anti-SCP3 (1:500,
396 ab97672, Abcam), anti-KIT (1:500, D13A2, Cell Signalling Technologies), anti-SOX9 (1:900,
397 5535, EMD Millipore), and anti-GPX4 (1:1,000, ab125066, Abcam). Sections were washed
398 using Tris-buffered saline containing 0.1% Tween20 (TBST). Antigen retrieval was performed
399 (except for anti-Kit) for 10 minutes in 0.01 M citrate buffer (pH 6.0) at 95°C. Afterwards, slides
400 were washed with TBST and blocked with 3% bovine serum albumin (BSA) and 0.3% Triton
401 X-100 in PBS for 1 hour at room temperature (RT). The slides were then incubated with
402 primary antibodies diluted in blocking solution overnight at 4°C, washed with TBST, and
403 incubated for 1 hour at RT with 4′,6-diamidino-2-phenylindole (DAPI, 1:1,000, Sigma) as well
404 as either a Cy3- or Alexa488-conjugated secondary antibody (1:500, Jackson
405 ImmunoResearch) or peanut agglutinin (PNA-Cy5, 1:2,000, Vector Laboratories) when
406 staining the acrosome for round spermatid identification. Sections were washed again with
407 TBST and mounted with Prolong Glass Antifade Mountant (Thermofisher). All images were
408 obtained using a confocal laser-scanning microscope (LSM800, Carl Zeiss) and processed in
409 Fiji (ImageJ).

410

411 **Cell death detection**

412 Apoptotic or non-apoptotic cell death was identified by double labelling for terminal
413 deoxynucleotidyl transferase dUTP nick end labelling (TUNEL, Merck Millipore) and an
414 antibody against active-caspase-3 (1:500, BD Biosciences). TUNEL labelling was performed
415 first and according to the manufacturer's instructions. In short, slides with testis sections were
416 washed in PBS and subjected to antigen retrieval by microwaving for 5 minutes in 0.01 M
417 citrate buffer. TdT mixture was applied and incubated at 37˚C for 1 hour, followed by
418 incubation with an anti-digoxigenin antibody conjugated with fluorescein at RT for 30 minutes.
419 Next, active-caspase-3 IHC was performed as described above with a slight modification:
420 instead of DAPI, Hoechst-44432 (1:5,000) was used. Using Fiji, male germ line cells in the
421 peripheral region of the seminiferous tissue and round spermatids in the luminal region were
422 independently quantified.

423

424 **Fluorescent *in situ* hybridization (FISH)**

425 FISH was performed according to a previously established protocol[54]. Slides with frozen
426 sections of the testis were subjected to antigen retrieval in Histo-VT One (Nacalai-Tesque) for

427 30 minutes at 90˚C and denatured using 50% formamide/2× saline-sodium citrate buffer (SSC),
428 followed by dehydration using 70% and 100% ethanol. A custom mixture of X (conjugated
429 with Cy3) and Y (conjugated with FITC) chromosome probes (Chromosome Science Labo)
430 was applied to the slides, covered with a hybridization cover (Hybrislip, Thermofisher) and
431 incubated at 80˚C for 10 minutes. Further hybridization occurred overnight in a humid chamber
432 at 37˚C. To enhance probe signals, IHC was performed. Samples were blocked using 5%
433 Blocking One solution (Nacalai-Tesque) for 1 hour at RT. Primary antibodies (anti-FITC,
434 1:2,000, A889, Invitrogen, and anti-Cy3, 1:2,000, sc-166894, Santa Cruz) were diluted in 5%
435 Blocking One solution and incubated for 1 hour at RT. After washing with 4× SSC, Cy3- or
436 Alexa488-conjugated secondary antibodies (1:2,000, Jackson ImmunoResearch) together with
437 Hoechst-44432 (1:5,000, Thermofisher) were applied and incubated for 1 hour at RT. Slides
438 were mounted with Prolong Glass Antifade Mountant (Thermofisher). All images were
439 obtained using a fluorescence microscope (Keyence BZ-X series) and processed in Fiji. RSs
440 were identified according to nuclear morphology and location within the tubule. Hybridization
441 efficiency was determined by microscopic evaluation and images were deemed appropriate for
442 analysis when, in more than 95% of cells, a sex chromosome could be assigned.
443
444 **Chemicals**
445 Butylated hydroxytoluene (BHT, Cat#W218405-1KG-K), ammonium acetate for LC-MS
446 LiChropur™ (Cat#5.33004) and dichloromethane (Cat#270997) were from Sigma-Aldrich.
447 EquiSPLASH™ (Cat#330731) and UltimateSPLASH® ONE Mass Spec Standard
448 (Cat#330820) were from Avanti Polar Lipids Inc. Methyl-tert-butyl ether (MTBE, Cat#34875),
449 ammonium formate (NH4HCO2, Cat#55674) and formic acid (Cat#94318) were from
450 Honeywell. Water (Cat#455), methanol (Cat#1428), acetonitrile (Cat#2697) and 2-propanol
451 (Cat#1178) were from CHEMSOLUTE®.
452
453 **Lipid extraction from whole testis for lipidomic analysis**
454 Lipid extraction from testes was performed using the methyl-tert-butyl ether (MTBE) method[55].
455 In short, approximately 100 mg of tissue was weighed into Precellys Lysing Kit tubes
456 (P000912-LYSK1-A, Bertin Technologies) and 1 mL methanol was added. Samples were kept
457 at 4˚C and homogenized using a Precellys® 24 homogenizer (5,500 rpm, 3 times for 30 seconds,
458 with a pause of 20 seconds between runs). Next, 500 µL of homogenate were transferred to a
459 10 mL screw-top glass vial (Chromacol 10-SV, Thermo) and spiked with internal standards
460 (50 µL EquiSPLASH™ diluted 1:100 and 50 µL UltimateSPLASH® ONE Mass Spec

461 Standard diluted 1:10, Avanti). Methanol (500 µL) and MTBE (3,330 µL) were added, and
462 samples were vortexed using an Ohaus Multi-Tube Vortex Mixer (2,500 rpm for 2 minutes,
463 pulsed), followed by incubation at 4˚C for 20 minutes. A second vortexing step was performed
464 (2,500 rpm for 2 minutes, pulsed) and samples were incubated at 4˚C for an additional 20
465 minutes. Ice-cold water (830 µL) was added, samples were vortexed (2,500 rpm for 3 minutes,
466 pulsed), and then centrifuged at 526 × g for 10 minutes at 4˚C. The upper phase was transferred
467 to a new screw-top vial. To the lower phase, MTBE (1,290 µL), methanol (388 µL), and water
468 (323 µL) were added for re-extraction, followed by vortexing (2,500 rpm for 3 minutes, pulsed)
469 and centrifugation at 526 × g for 10 minutes at 4˚C. Upper phases were combined and
470 evaporated to dryness using a RapidVap (Labconco) with the following settings: 45% speed,
471 35˚C, 250 mbar for 30 minutes; 45% speed, 35˚C, 150 mbar for 20 minutes; and 45% speed,
472 40˚C, 50 mbar for 50 minutes. Dried extracts were resuspended in 200 µL 2-propanol and
473 transferred to an amber 300 µL fixed insert vial (Chromacol 03-FIRV(A), Thermo) for LC–
474 MS/MS analysis. A pooled sample was prepared by combining 7.5 µL of each extract. All
475 solvents were supplemented with 0.01% (w/v) butylated hydroxytoluene (BHT) and cooled on
476 ice prior to lipid extraction.
477
478 **Lipidomic analysis**
479 Lipidomics was performed using hydrophilic interaction chromatography (HILIC) coupled to
480 triple quadrupole mass spectrometry. HILIC was carried out on a SCIEX Triple Quad™ 7500
481 system equipped with a Luna® NH2 column (100 × 2 mm; 3 µm, 100 Å, Phenomenex). Lipids
482 were separated by gradient elution using solvent A (acetonitrile/dichloromethane, 93:7, v/v)
483 and solvent B (acetonitrile/water, 50:50, v/v), both containing 5 mM ammonium acetate.
484 Solvent B was adjusted to pH 8.2 with NH3 (15%). Separation was performed at 35˚C using
485 the following gradient: 0 to 2 minutes, 0% B isocratic (flow rate 0.2 mL/min); 2 to 11 minutes,
486 0% to 40% B (flow rate 0.5 mL/min); 11 to 11.5 minutes, 40% to 70% B (flow rate 0.5
487 mL/min); 11.5 to 12.5 minutes, 70% to 100% B (flow rate 0.5 mL/min); 12.5 to 15 minutes,
488 100% B isocratic (flow rate 0.5 mL/min); 15 to 15.1 minutes, 100% to 0% B, followed by re-
489 equilibration at 0% B for 2.5 minutes. The triple quadrupole mass spectrometer was operated
490 with the following settings: TEM 500˚C, GS1 45, GS2 70, CUR 45, CAD 9, IS −3,500 V. Data
491 were acquired in multiple reaction monitoring (MRM) mode using a published assay (SCIEX
492 technical note RUO-MKT-02-8477-C). For quantification, the area under the curve for each
493 precursor mass to fragment mass transition was integrated using SCIEX OS software and
494 normalized to appropriate internal standards from UltimateSPLASH® ONE (Avanti),

495 including PC(17:0_22:4(d5)), PE(17:0_18:1(d5)), LPC(17:0(d5)), and LPE(17:0(d5)). Isotopic
496 correction was performed using LICAR[56].
497
498 **Round spermatid (RS) isolation**
499 Isolation was carried out according to a previously established protocol[57]. Briefly, Fresh
500 testicular tissue was harvested from young or aged male mice followed by removal of the
501 epididymis and tunica albuginea. A single cell suspension was obtained via serial digestion
502 with Collagenase IV (1mg/ml, Sigma) and Trypsin (0.6 mg/ml, Worthington) / DNAse I (>3.2
503 kU/ml, Sigma) dissolved in Krebs bicarbonate buffer. The cell suspension was loaded on a 1-
504 5% BSA / Krebs buffer gradient and allowed to sediment for 1.5 hour on ice at 1 unit gravity.
505 Twenty-eight fractions of 1 mL were collected and analyzed for purity using PNA (1:2,000,
506 Rhodamine, Vector Laboratories) and DAPI (1:1,000, Sigma). Only fractions #4-7 were
507 routinely enriched with RSs (>80%, Extended Data Fig. 3). Therefore, in subsequent isolations,
508 fractions #4-7 were collected and pooled. The fractions were washed with Krebs buffer to
509 remove excess BSA and immediately used for RNA and protein isolation.
510
511 **Simultaneous RNA and Protein isolation**
512 RNA and protein were simultaneously isolated using the AllPrep DNA/RNA/Protein mini kit
513 (Qiagen) according to the manufacturer's protocol, with one minor modification: the protein
514 fraction was air dried and then vortexed for 1 minute in SDS buffer (containing 4% SDS, 20%
515 sucrose, 10 mM Tris-HCl pH 6.8 and 1× ethylenediaminetetraacetic acid (EDTA)-free protease
516 inhibitor (Roche), followed by incubation at 37˚C for 30 minutes. The protein sample was
517 vortexed and pelleted via centrifugation. Supernatant was transferred to a new tube and protein
518 concentration was determined using the bicinchoninic acid assay (BCA, Nacalai-Tesque).
519 RNA was assessed for concentration and purity using the Nanodrop (Thermofisher). Isolated
520 RNA and protein were stored at -80˚C until further use.
521
522 **cDNA synthesis and quantitative polymerase chain reaction (qPCR)**
523 RNA isolated from pooled round spermatid fractions (1 µg) was reverse transcribed into cDNA
524 using the SuperScript III™ First-Strand Synthesis System for RT-PCR (Invitrogen). cDNA (2
525 µl, 1:10 diluted) was subsequently used for qPCR using Taq Pro Universal SYBR qPCR Master
526 Mix (Vazyme). Primer sequences used in this study can be found in Extended Data Table 2.
527 Assay specificity was verified by single-peak melt curves and a single band of the expected
528 size on agarose gel. For *Gpx4* transcript analysis, three qPCR assays were used[39]: a primer set

529 specific for the *nGpx4* transcript, a primer set specific for the mitochondrial-targeted *Gpx4*
530 transcript (*mGpx4*), and a primer set amplifying a region shared by mitochondrial and cytosolic
531 transcripts (*mGpx4*+*cGpx4*). Ct values were normalized to *ActB* (ΔCt). To estimate the
532 cytosolic component, expression values were converted to linear scale ($2^{-\Delta Ct}$), and cytosolic
533 expression was calculated as $\boldsymbol{E_c} = \boldsymbol{E_{m+c}} - E_m$, where $\boldsymbol{E_{m+c}}$ is the signal from the assay
534 amplifying the shared mitochondrial+cytosolic transcripts and E_m is the mitochondrial-specific
535 assay. Group comparisons were performed on log2-transformed expression values.
536
537 **Western blot**
538 Protein samples (5 µg) were separated by SDS-PAGE on 12% TGX™ FastCast™ acrylamide
539 gels (Bio-Rad) at 150 V for 50 minutes and transferred to 0.2 µm polyvinylidene difluoride
540 (PVDF) membranes (Trans-Blot Turbo Mini PVDF Transfer Packs; Bio-Rad) using the Trans-
541 Blot Turbo system (2.5 A, 25 V, 3 minutes). Membranes were blocked in 10% Intercept TBS
542 blocking buffer (Licor; GPX4, ActB), 5% Blocking One (Nacalai-Tesque; 4HNE, GAPDH),
543 or 5% skimmed milk in TBST (FTH1, FTL and NCOA4) and incubated overnight at 4˚C with
544 primary antibodies against GPX4 (1:1,000, ab125066, Abcam), 4HNE, (1:1,000, ab46545,
545 Abcam), ACTB (1:2,500, sc-47778, Santa Cruz), GAPDH (1:4,000, ab8245, Abcam), FTH1
546 (1:1,000, ab183781, abcam) FTL (1:1,000, ab69090, abcam) and NCOA4 (1:1,000, ab314553,
547 abcam). After washing with Tris-buffered saline containing 0.1% Tween-20 (TBST),
548 membranes were incubated for 1 hour at room temperature with HRP-conjugated secondary
549 antibodies: for GPX4 and ACTB, W4011 (1:10,000) and W4021 (1:5,000) in 10% Intercept;
550 for 4HNE and GAPDH, both 1:10,000 in 5% Blocking One; and for FTH1, FTL and NCOA4,
551 both 1:10,000 in 'Can Get Signal?' (Toyobo). Membranes were washed again in TBST, and
552 signals were visualized using a ChemiDoc Touch Imaging System (Bio-Rad). Band intensities
553 were quantified in Fiji and normalized to ACTB or GAPDH as specified.
554
555 **Flow cytometric analysis of mature sperm**
556 The caudal epididymis was excised from two testes, incised 4 times, and transferred to a dish
557 containing 2 mL prewarmed (37°C) phosphate buffered saline (PBS) with 2% FBS. Viable
558 mature sperm were allowed to swim out into the medium for 10 minutes in a 37˚C, 5.0% CO_2
559 incubator. The sperm suspension was filtered through a 40 µm PET cell strainer and stained
560 with Hoechst (5 µg/mL) for 45 minutes at 35°C in the dark, mixing every 15 minutes. Samples
561 were kept on ice until analysis, which proceeded within 1 hour. Directly before analysis, 2 mL
562 cell suspensions were filtered through a 35 µm strainer cap attached to a 5 mL Polystyrene

563 Round Bottom FACS tube (Falcon). Cells were subjected to flow cytometry using an
564 LSRFortessa cell analyzer (BD Biosciences). Hoechst was excited using the 355 nm UV laser
565 and detected using a 450/50 bandpass filter. Forward Scatter (FSC) and Side Scatter (SSC)
566 were detected using a 488 nm laser and a 488/10 bandpass filter. Flow rate was set to achieve
567 2,500-3,500 events/second. A minimum of 100,000 events within a specified gate (Fig 3d)
568 were recorded using the BD FACSDiva Software (BD Biosciences). Data analysis was done
569 using FlowJo software v10.10.0 (BD Life Sciences).
570
571 **Statistical analysis**
572 Statistical information for individual experiments is shown in the corresponding figure
573 legends. Values are presented as mean ± standard deviation. Data were first analysed for
574 normality using the Shapiro–Wilk test. Depending on distribution and variance, statistical
575 comparisons between groups were performed using Student's *t*-test, Welch's *t*-test, or the
576 Mann–Whitney *U* test. Longitudinal effects were analysed using two-way ANOVA (fixed
577 effects: diet, week and bodyweight; random effect: individual mouse, repeated measures).
578 Results were considered significant at $P < 0.05$. Statistical analyses were conducted using
579 GraphPad Prism 10 (GraphPad Software).

Declaration of interest

The authors declare no conflict of interest.

Acknowledgements

We thank the Japanese Society for the Promotion of Science KAKENHI grant number #17K19372, #22K19322, and #25K22536, The Canon Foundation awarded to N.O., the establishment of university fellowships towards the creation of science technology innovation, grant number JPMJFS2102, JPMJSP2114 awarded to J.G., and JST FOREST Program (JPMJFR2213) awarded to E.M. for financial support. M.C. received funding from the European Research Council (ERC) under the European Union's Horizon 2020 research and innovation program (grant agreement no. GA 884754). We thank Sayaka Makino and Asuka Takehara for animal care and all other members of the Developmental Neuroscience laboratory at Tohoku University for their useful comments. We also thank Prof. Junken Aoki (Graduate School of Pharmaceutical Sciences, The University of Tokyo) for advice on lipidomic analysis and Dr. Ibuki Kusumoto (Laboratory of Food Function Analysis, Tohoku University) for technical support.

Author contributions

Study design: J.G., T.K., W.G., E.M., N.O.; Data collection: J.G., T.K., J.I., L.G., B.H.; Data analysis: J.G.; J.I., B.H., M.A.; Drafted the manuscript: J.G.; Edited the manuscript: T.K., W.G., E.M., M.C., N.O.; Funding acquisition: J.G., E.M., M.C., N.O.

Competing interests

M.C. is co-founder and shareholder of ROSCUE Therapeutics GmbH. The other authors declare no competing interests.

605 **References**

606 1. Johnson, S. L., Dunleavy, J., Gemmell, N. J. & Nakagawa, S. Consistent age-
607 dependent declines in human semen quality: A systematic review and meta-analysis.
608 *Ageing Res. Rev.* **19**, 22–33 (2015).
609 2. Verón, G. L. *et al.* Impact of age, clinical conditions, and lifestyle on routine semen
610 parameters and sperm kinematics. *Fertil. Steril.* **110**, 68-75.e4 (2018).
611 3. Evenson, D. P., Djira, G., Kasperson, K. & Christianson, J. Relationships between the
612 age of 25,445 men attending infertility clinics and sperm chromatin structure assay
613 (SCSA®) defined sperm DNA and chromatin integrity. *Fertil. Steril.* **114**, 311–320
614 (2020).
615 4. Martins da Silva, S. & Anderson, R. A. Reproductive axis ageing and fertility in men.
616 *Rev. Endocr. Metab. Disord.* **23**, 1109–1121 (2022).
617 5. Griswold, M. D. Spermatogenesis: The Commitment to Meiosis. *Physiol. Rev.* **96**, 1–
618 17 (2016).
619 6. Gosden, R. G., Richardson, D. W., Brown, N. & Davidson, D. W. Structure and
620 gametogenic potential of seminiferous tubules in ageing mice. *Reproduction* **64**, 127–
621 133 (1982).
622 7. Wright, W. W., Fiore, C. & Zirkin, B. R. The effect of aging on the seminiferous
623 epithelium of the brown Norway rat. *J. Androl.* **14**, 110–7 (1993).
624 8. Silva, J. V. *et al.* Effects of Age and Lifelong Moderate-Intensity Exercise Training on
625 Rats' Testicular Function. *Int. J. Mol. Sci.* **23**, 11619 (2022).
626 9. Dong, S. *et al.* Testicular aging, male fertility and beyond. *Front. Endocrinol.*
627 *(Lausanne).* **13**, (2022).
628 10. Nguyen-Powanda, P. & Robaire, B. Oxidative Stress and Reproductive Function in the
629 Aging Male. *Biology (Basel).* **9**, 282 (2020).
630 11. Gunes, S., Hekim, G. N. T., Arslan, M. A. & Asci, R. Effects of aging on the male
631 reproductive system. *J. Assist. Reprod. Genet.* **33**, 441–454 (2016).
632 12. Villalpando-Rodriguez, G. E. & Gibson, S. B. Reactive Oxygen Species (ROS)
633 Regulates Different Types of Cell Death by Acting as a Rheostat. *Oxid. Med. Cell.*
634 *Longev.* **2021**, 9912436 (2021).
635 13. Blanco-Rodríguez, J. & Martínez-García, C. Spontaneous germ cell death in the testis
636 of the adult rat takes the form of apoptosis: re-evaluation of cell types that exhibit the
637 ability to die during spermatogenesis. *Cell Prolif.* **29**, 13–31 (1996).

638 14. Bromfield, E. G. *et al.* Differential cell death decisions in the testis: evidence for an
639 exclusive window of ferroptosis in round spermatids. *MHR: Basic science of*
640 *reproductive medicine* **25**, 241–256 (2019).
641 15. Oresti, G. M. *et al.* Differentiation-related changes in lipid classes with long-chain and
642 very long-chain polyenoic fatty acids in rat spermatogenic cells. *J. Lipid Res.* **51**,
643 2909–2921 (2010).
644 16. Li, Z., Lange, M., Dixon, S. J. & Olzmann, J. A. Lipid Quality Control and
645 Ferroptosis: From Concept to Mechanism. *Annu. Rev. Biochem.* **93**, 499–528 (2024).
646 17. Matzkin, M. E., Calandra, R. S., Rossi, S. P., Bartke, A. & Frungieri, M. B. Hallmarks
647 of Testicular Aging: The Challenge of Anti-Inflammatory and Antioxidant Therapies
648 Using Natural and/or Pharmacological Compounds to Improve the Physiopathological
649 Status of the Aged Male Gonad. *Cells* **10**, (2021).
650 18. Dixon, S. J. *et al.* Ferroptosis: An Iron-Dependent Form of Nonapoptotic Cell Death.
651 *Cell* **149**, 1060–1072 (2012).
652 19. Mishima, E. *et al.* Recommendations for robust and reproducible research on
653 ferroptosis. *Nat. Rev. Mol. Cell Biol.* **26**, 615–630 (2025).
654 20. Dixon, S. J. & Olzmann, J. A. The cell biology of ferroptosis. *Nat. Rev. Mol. Cell Biol.*
655 **25**, 424–442 (2024).
656 21. Friedmann Angeli, J. P. *et al.* Inactivation of the ferroptosis regulator Gpx4 triggers
657 acute renal failure in mice. *Nat. Cell Biol.* **16**, 1180–1191 (2014).
658 22. Yang, W. S. *et al.* Regulation of Ferroptotic Cancer Cell Death by GPX4. *Cell* **156**,
659 317–331 (2014).
660 23. Doll, S. *et al.* ACSL4 dictates ferroptosis sensitivity by shaping cellular lipid
661 composition. *Nat. Chem. Biol.* **13**, 91–98 (2017).
662 24. Galy, B., Conrad, M. & Muckenthaler, M. Mechanisms controlling cellular and
663 systemic iron homeostasis. *Nat. Rev. Mol. Cell Biol.* **25**, 133–155 (2024).
664 25. Conrad, M. & Pratt, D. A. The chemical basis of ferroptosis. *Nat. Chem. Biol.* **15**,
665 1137–1147 (2019).
666 26. Saito, H., Hara, K., Kitajima, S. & Tanemura, K. Effect of vitamin E deficiency on
667 spermatogenesis in mice and its similarity to aging. *Reproductive Toxicology* **98**, 225–
668 232 (2020).
669 27. Bensoussan, K., Morales, C. R. & Hermo, L. Vitamin E deficiency causes incomplete
670 spermatogenesis and affects the structural differentiation of epithelial cells of the
671 epididymis in the rat. *J. Androl.* **19**, 266–88 (1998).

672 28. Endo, T. *et al.* Multiple ageing effects on testicular/epididymal germ cells lead to
673 decreased male fertility in mice. *Commun. Biol.* **7**, 16 (2024).
674 29. Chen, Y.-F. *et al.* Cisd2 deficiency drives premature aging and causes mitochondria-
675 mediated defects in mice. *Genes Dev.* **23**, 1183–1194 (2009).
676 30. Luo, L. *et al.* Aging and the Brown Norway Rat Leydig Cell Antioxidant Defense
677 System. *J. Androl.* **27**, 240–247 (2006).
678 31. Liao, C.-H. *et al.* Optimizing a Male Reproductive Aging Mouse Model by d-
679 Galactose Injection. *Int. J. Mol. Sci.* **17**, 98 (2016).
680 32. Kimura, A. K. & Kim, H.-Y. Phosphatidylserine synthase 2: high efficiency for
681 synthesizing phosphatidylserine containing docosahexaenoic acid. *J. Lipid Res.* **54**,
682 214–222 (2013).
683 33. Sulc, A. *et al.* MALDI Imaging Mass Spectrometry Reveals Lipid Alterations in
684 Physiological and Sertoli Cell-Only Syndrome Human Testicular Tissue Sections. *Int.*
685 *J. Mol. Sci.* **25**, (2024).
686 34. Braverman, N. E. & Moser, A. B. Functions of plasmalogen lipids in health and
687 disease. *Biochimica et Biophysica Acta (BBA) - Molecular Basis of Disease* **1822**,
688 1442–1452 (2012).
689 35. Imai, H. *et al.* Depletion of Selenoprotein GPx4 in Spermatocytes Causes Male
690 Infertility in Mice. *Journal of Biological Chemistry* **284**, 32522–32532 (2009).
691 36. Schneider, M. *et al.* Mitochondrial glutathione peroxidase 4 disruption causes male
692 infertility. *The FASEB Journal* **23**, 3233–3242 (2009).
693 37. Conrad, M. *et al.* The Nuclear Form of Phospholipid Hydroperoxide Glutathione
694 Peroxidase Is a Protein Thiol Peroxidase Contributing to Sperm Chromatin Stability.
695 *Mol. Cell. Biol.* **25**, 7637–7644 (2005).
696 38. Mishima, E. *et al.* DHODH inhibitors sensitize to ferroptosis by FSP1 inhibition.
697 *Nature* **619**, E9–E18 (2023).
698 39. Borchert, A. *et al.* The Role of Phospholipid Hydroperoxide Glutathione Peroxidase
699 Isoforms in Murine Embryogenesis. *Journal of Biological Chemistry* **281**, 19655–
700 19664 (2006).
701 40. Ngo, V. & Duennwald, M. L. Nrf2 and Oxidative Stress: A General Overview of
702 Mechanisms and Implications in Human Disease. *Antioxidants (Basel).* **11**, (2022).
703 41. Lasiene, K. *et al.* Age-related morphological peculiarities of human testes. *Folia*
704 *Morphol. (Warsz).* **80**, 122–126 (2021).

705 42. Jiang, H. *et al.* Quantitative histological analysis and ultrastructure of the aging human
706 testis. *Int. Urol. Nephrol.* **46**, 879–885 (2014).
707 43. Barnes, C. J., Covington, B. W. & Lee, M. Effect of Aging and Dietary Restriction on
708 Rat Testicular Germ Cell Apoptosis. *J. Gerontol. A Biol. Sci. Med. Sci.* **54**, B199–
709 B204 (1999).
710 44. Morales, E. *et al.* Effect of ageing on the proliferation and apoptosis of testicular germ
711 cells in the Syrian hamster Mesocricetus auratus. *Reprod. Fertil. Dev.* **15**, 1–10 (2003).
712 45. Mortensen, M. S., Ruiz, J. & Watts, J. L. Polyunsaturated Fatty Acids Drive Lipid
713 Peroxidation during Ferroptosis. *Cells* **12**, (2023).
714 46. Kagan, V. E. *et al.* Oxidized arachidonic and adrenic PEs navigate cells to ferroptosis.
715 *Nat. Chem. Biol.* **13**, 81–90 (2017).
716 47. Sutovsky, P. *et al.* A putative, ubiquitin-dependent mechanism for the recognition and
717 elimination of defective spermatozoa in the mammalian epididymis. *J. Cell Sci.* **114**,
718 1665–1675 (2001).
719 48. Cocquet, J. *et al.* A Genetic Basis for a Postmeiotic X Versus Y Chromosome
720 Intragenomic Conflict in the Mouse. *PLoS Genet.* **8**, e1002900 (2012).
721 49. Braun, R. E., Behringer, R. R., Peschon, J. J., Brinster, R. L. & Palmiter, R. D.
722 Genetically haploid spermatids are phenotypically diploid. *Nature* **337**, 373–376
723 (1989).
724 50. Bhutani, K. *et al.* Widespread haploid-biased gene expression enables sperm-level
725 natural selection. *Science (1979).* **371**, (2021).
726 51. You, Y.-A. *et al.* Sex chromosome-dependent differential viability of human
727 spermatozoa during prolonged incubation. *Human Reproduction* **32**, 1183–1191
728 (2017).
729 52. Rahman, M. S. & Pang, M.-G. New Biological Insights on X and Y Chromosome-
730 Bearing Spermatozoa. *Front. Cell Dev. Biol.* **7**, 388 (2019).
731 53. Kimura, R., Yoshizaki, K. & Osumi, N. Dynamic expression patterns of Pax6 during
732 spermatogenesis in the mouse. *J. Anat.* **227**, 1–9 (2015).
733 54. Tatehana, M., Kimura, R., Mochizuki, K., Inada, H. & Osumi, N. Comprehensive
734 histochemical profiles of histone modification in male germline cells during meiosis
735 and spermiogenesis: Comparison of young and aged testes in mice. *PLoS One* **15**,
736 e0230930 (2020).

55. Matyash, V., Liebisch, G., Kurzchalia, T. V., Shevchenko, A. & Schwudke, D. Lipid extraction by methyl-tert-butyl ether for high-throughput lipidomics. *J. Lipid Res.* **49**, 1137–1146 (2008).

56. Gao, L. *et al.* LICAR: An Application for Isotopic Correction of Targeted Lipidomic Data Acquired with Class-Based Chromatographic Separations Using Multiple Reaction Monitoring. *Anal. Chem.* **93**, 3163–3171 (2021).

57. Da Ros, M., Lehtiniemi, T., Olotu, O., Meikar, O. & Kotaja, N. Enrichment of Pachytene Spermatocytes and Spermatids from Mouse Testes Using Standard Laboratory Equipment. *Journal of Visualized Experiments* https://doi.org/10.3791/60271 (2019) doi:10.3791/60271.

750 **Fig. 1: Age-related alterations in mouse testis germ cell populations.**
751 **a**–**c**, Body weight (**a**), combined testes weight (**b**) and gonadosomatic index (combined testes
752 weight/body weight; **c**) in young (3 months) and aged (18 months) males. **d**, Schematic of
753 spermatogenesis highlighting undifferentiated and differentiating spermatogonia, pachytene
754 spermatocytes, round spermatids (RSs) and spermatozoa. **e**, Representative stage VII–VIII
755 seminiferous tubules stained for PLZF (undifferentiated spermatogonia), KIT (differentiating
756 spermatogonia), SCP3 (pachytene spermatocytes), PNA (RSs) and SOX9 (Sertoli cells); nuclei
757 counterstained with DAPI. Scale bar, 50 µm. f–j, Quantification of PLZF$^+$ (**f**), KIT$^+$ (**g**), SCP3$^+$
758 (**h**), PNA$^+$ (**i**) and SOX9$^+$ (**j**) cells, normalized to tubule circumference (**f**: 20 images per mouse;
759 **g**–**j**: 10 images per mouse). **k**, Representative tubules showing CASP3$^+$/TUNEL$^+$ and
760 CASP3$^-$/TUNEL$^+$ events in peripheral and luminal compartments; nuclei counterstained with
761 Hoechst. Scale bar, 50 µm. **l**–**o**, Quantification of CASP3$^+$/TUNEL$^+$ and CASP3$^-$/TUNEL$^+$
762 cells in the periphery (**l**, **m**) and lumen (**n**, **o**), normalized to 100 tubules. Data are mean ± s.d.;
763 dots represent mice. Statistics: two-tailed Student's *t*-test (**a**–**c**, **f**, **h**, **i**, **l**, **n**, **o**) or Mann–Whitney
764 *U* test (**g**, **j**, **m**), exact *P* values are given. *N* = 6 mice per group. Illustration in **d** was created in
765 BioRender, Germeraad, J. (2026) https://BioRender.com/8iim1z1
766
767 **Fig. 2: Increased lipid peroxidation in aged whole testis and round spermatids.**
768 **a**, Workflow for isolation of RS-enriched fractions and extraction of RNA/protein using a
769 modified density-gradient approach. **b**, Representative immunoblots of 4HNE adducts and
770 quantification, normalized to GAPDH, black triangle indicates quantified band. **c**–**h**, RS
771 mRNA expression of *Alox15* (**c**), *Acsl4* (**d**), *Acsl6* (**e**) and *Gpx4* isoforms (*nGpx4* (**f**), *mGpx4*
772 (**g**), *cGpx4* (**h**)), shown as fold change relative to *ActB*. **i**, Representative immunoblots and
773 quantification of GPX4 protein, normalized to ACTB. **j**, Schematic outlining NRF2 activation
774 and initiating its target gene expression. Oxidative stress activates NRF2 ,via KEAP1 release,
775 to induce antioxidant/HO-1 programs, while iron uptake (TFR1), storage (FTH1/FTL), and
776 ferritinophagy (NCOA4) regulate the labile iron pool (LIP) **k**–**o**, RS mRNA expression of *Nrf2*
777 (**k**), *Sod1* (**l**), *Cat* (**m**), *HO-1* (**n**) and *Tfr1* (**o**), relative to *ActB*. **p**–**s**, Representative
778 immunoblots (**p**) and quantification of FTH1 (**q**), FTL (**r**) and NCOA4 (**s**). **t**, Summary
779 schematic of aging-associated changes across lipid peroxidation, redox defence and iron
780 metabolism (red, increased; blue, decreased; gray boxes, protein; white boxes, mRNA). Data
781 are mean ± s.d.; dots represent mice. Statistics: Welch's *t*-test (**a**); two-tailed Student's *t*-test
782 (**b**–**e**, **g**–**i**, **k**, **l**, **n**, **q**–**s**); Mann–Whitney *U* test (**f**, **m**, **o**), exact P values are given. *N* = 6 mice
783 per group.

784

785 **Fig. 3: Aging alters the sex chromosome ratio in round spermatids and mature sperm.**
786 **a**, **b**, FISH in RSs showing Y-chromosomes (green; closed arrowhead) and X-chromosomes
787 (red; open arrowhead) signals with Hoechst counterstain (**a**) and quantification of Y/X ratio
788 (Young: n = 6,282±100 Y-RSs, *n* = *6*,188±113 X-RSs; mean Y/X ratio 1.02; Aged: *n* =
789 6,694±85 Y-RSs, *n* = 6,056±98 X-RSs; mean Y/X ratio 1.11) (**b**). Scale bar, 5 µm. **c**, Sperm
790 collection and DNA staining workflow: cauda epididymides were excised and sperm was
791 collected via swim-out (37 °C, 10 min) followed by Hoechst 33342 staining (45 min) before
792 flow cytometry. **d**, Gating strategy to resolve X- and Y-bearing sperm: debris exclusion (FSC-
793 A vs SSC-A), singlet selection (FSC-H vs FSC-W and Hoechst Blue vs SSC-A), and
794 histogram-based separation by Hoechst Blue intensity. **e**, **f**, Representative Hoechst Blue
795 distributions (young vs aged and overlay normalized to mode) (**e**) and Y/X ratio quantification
796 (young: *n* = 3,382,147 ± 140,662 Y-sperm vs *n* = 3,293,224 ± 126,522 X-sperm; mean Y/X
797 1.02; aged: *n* = 3,294,779 ± 156,878 Y-sperm; *n* = 3,032,412 ± 145,748 X-sperm; mean Y/X
798 1.09) (**f**). Data are mean ± s.d.; dots represent mice. Statistics: two-tailed Student's t-test (**b**, **f**).
799 Exact *P* values are shown. *N* = 6 mice per group. Illustration in **c** was created in BioRender,
800 Germeraad, J. (2026) https://BioRender.com/j1osdbj

801

802 **Fig. 4: Vitamin E deficient feeding recapitulates age-associated testis phenotypes.**
803 **a**, Experimental design: young males (1 month) fed control or vitamin E–deficient diet (VE(−))
804 for 70 days. **b**, body weight was recorded weekly for 10 weeks in the same cohort of mice. **c,**
805 **d,** combined testes weight (**c**) and gonadosomatic index (combined testes weight/body weight;
806 **d**). **e**, Representative stage VII–VIII seminiferous tubules stained for PLZF, KIT, SCP3, PNA
807 and SOX9: counterstained with DAPI. **f**–**j**, Quantification of $PLZF^+$ (**f**), KIT^+ (**g**), $SCP3^+$ (**h**),
808 PNA^+ (**i**) and $SOX9^+$ (**j**) cells, normalized to tubule circumference (**f**: 20 images per mouse; **g**–
809 **j**: 10 images per mouse). **k**, Representative tubules showing $CASP3^+/TUNEL^+$ cells in the
810 periphery and $CASP3^-/TUNEL^+$ cells in the lumen. **l**, **m**, Quantification of $CASP3^+/TUNEL^+$
811 and $CASP3^-/TUNEL^+$ cells in peripheral (**l**) and luminal compartments (**m**). **n**, qPCR of fatty-
812 acid metabolism, GPX4 defence, NRF2-response and iron-homeostasis transcripts, relative to
813 ActB. **o**, **p**, Representative immunoblots and quantification of 4HNE (**o**) and GPX4 (**p**),
814 normalized to GAPDH, black triangle indicates quantified band. **q**–**t**, Representative
815 immunoblots (**q**) and quantification of FTH1 (**r**), FTL (**s**) and NCOA4 (**t**). **u**, FISH in RSs with
816 X (red) or Y (green) signals and Y/X ratio (control: *n* = 6,390±125 Y-RSs vs *n* = 6,274±127
817 X-RSs; mean Y/X ratio 1.02; VE(−): *n* = 6,548±222 Y-RSs vs *n* = 6,186±212 X-RSs; mean

818 Y/X ratio 1.09). Scale bars: **e**, 50 µm (overview) and 5 µm (inset); **k**, 50 µm; **u**, 5 µm. Data are
819 mean ± s.d.; dots represent mice except for **b** where it represents the mean of each group.
820 Statistics: two-way repeated measures-ANOVA with Geisser–Greenhouse correction (**b**); two-
821 tailed Student's *t*-test (**c**, **d**, **f**–**i**, **m**–**p**, **r**–**t**, **u**); Mann–Whitney *U* test (**j**, **l**, **n**), exact *P* values are
822 given. Sample sizes: **b**–**d**, $N = 9$ per group; all other panels, $N = 6$ per group.
823
824 **Fig. 5: Vitamin E supplemented feeding rescues age-associated phenotypes within the**
825 **testis.**
826 **a**, Experimental design: aged (16-months) males fed control or vitamin E–supplemented diet
827 (VE+) for 70 days. **b**, body weight was recorded weekly for 10 weeks in the same cohort of
828 mice. **c**, **d**, combined testes weight (**c**) and gonadosomatic index (combined testes weight/body
829 weight; **d**). **e**, Representative stage VII–VIII seminiferous tubules stained for PLZF, KIT, SCP3,
830 PNA and SOX9: nuclei counterstained with DAPI. **f**–**j**, Quantification of $PLZF^+$ (**f**), KIT^+ (**g**),
831 $SCP3^+$ (**h**), PNA^+ (**i**) and $SOX9^+$ (**j**) cells, normalized to tubule circumference (**f**: 20 images
832 per mouse; **g**–**j**: 10 images per mouse). **k**, Representative tubules showing $CASP3^+/TUNEL^+$
833 peripheral and $CASP3^-/TUNEL^+$ luminal events. **l**,**m**, Quantification of $CASP3^+/TUNEL^+$ and
834 $CASP3^-/TUNEL^+$ cells in peripheral (**l**) and luminal compartments (**m**). **n**, qPCR of fatty-acid
835 metabolism, GPX4 defence, NRF2-response and iron-homeostasis transcripts, relative to ActB.
836 **o**, **p**, Representative immunoblots and quantification of 4HNE (**o**) and GPX4 (**p**), normalized
837 to GAPDH, black triangle indicates quantified band. **q**–**t**, Representative immunoblots (**q**) and
838 quantification of FTH1 (**r**), FTL (**s**) and NCOA4 (**t**). **u**, FISH in RSs with X (red) or Y (green)
839 signals and Y/X ratio (control: $n = 6{,}527 \pm 135$ Y-RSs vs $n = 5{,}950 \pm 156$ X-RSs; Y/X ratio mean
840 1.10; VE(+): $n = 5{,}772 \pm 156$ Y-RSs vs $n = 5{,}702 \pm 149$ X-RSs; mean Y/X ratio 1.01). Scale bars:
841 **e**, 50 µm (overview) and **5** µm (inset); **k**, 50 µm; **u**, 5 µm. Data are mean ± s.d.; dots represent
842 mice except for **b** where it represents the mean of each group. Statistics: two-way repeated
843 measures-ANOVA with Geisser–Greenhouse correction (**b**); two-tailed Student's *t*-test (**c**, **f**, **g**,
844 **i**, **l**, **m**, **n**, **p**, **r**, **s**, **u**); Welch's *t*-test (**o**); Mann–Whitney *U* test (**d**, **h**, **j**, **t**), exact *P* values are
845 given. Sample sizes: **b**–**d**, $N = 9$ per group; all other panels, $N = 6$ per group.
846
847 **Extended data Fig. 1: Age-associated cell death is increased in seminiferous tubules**
848 **a**, Representative images of tubules containing $TUNEL^+$ cells in young and aged mice.
849 Asterisks indicate tubules containing $TUNEL^+$ cells. Scale bar: 200 µm. **b**, Percentage of
850 seminiferous tubules containing cells $TUNEL^+$ cells relative to the total number of tubules
851 within a section. **c**, Representative images of $CASP3^+/TUNEL^+$ round spermatids in young and

852 aged testis sections. Scale bar: 50µm. Data is presented as mean ± s.d. Significance was
853 determined by two-tailed Student's *t*-test (**b**). Exact *P* value is given. Sample size: *N* = 6 in
854 each group. Each dot represents one mouse.
855
856 **Extended data Fig. 2: Aging shifts phosphatidylcholine composition toward plasmalogen**
857 **PC**
858 **a-d**, Heatmaps showing relative abundances of individual phospholipid species in young and
859 aged whole testis: diacyl phosphatidylcholine (PC; **a**), diacyl phosphatidylethanolamine (PE;
860 **b**), plasmalogen phosphatidylcholine (PCp; **c**) and plasmalogen phosphatidylethanolamine
861 (PEp; **d**). Columns represent biological replicates and rows represent lipid species. Values are
862 scaled to show relative differences across samples. **e**, **f**, mRNA level quantification analysis of
863 *Elovl2* (**e**) and *Elovl5* (**f**) expression in young and aged round spermatids. Data is presented as
864 mean ± s.d. Significance was determined by two-tailed Student's *t*-test (**e, f**). Sample size: *N* =
865 6 in each group. Each dot represents one mouse.
866
867 **Extended data Fig. 3: Enrichment profile of round spermatids across fractions.**
868 **a,** Representative image of the enriched cell suspension (fraction #3) stained with peanut
869 agglutinin (PNA) to label the acrosome and DAPI to label nuclei. Scale bar: 20µm. **b,**
870 Representative cellular composition of fractions showing the percentage of round spermatids
871 versus other germ-cell populations (including spermatogonia and other cells). Each bar
872 represents one fraction; stacked colors indicate the relative contribution of round spermatids
873 (orange) and other cells (green).
874
875 **Extended data Fig. 4: GPX4 localization and ferritin expression in testicular aging**
876 **a,** Representative images of GPX4 localization in seminiferous tubules from young and aged
877 testes, with DAPI counterstain. Scale bar: 50µm. **b, c,** mRNA level quantification of iron-
878 handling transcripts in round spermatids from young and aged mice: *Fth1* (**b**) and *Ftl* (**c**),
879 relative to *ActB*. Data are presented as mean ± s.d. Significance was determined by two-tailed
880 Student's *t*-test (**b, c**). Exact *P* values are given. Sample size: *N* = 6 in each group. Each dot
881 represents one mouse.
882
883 **Extended data Fig. 5: Dietary vitamin E modulates cell death in young and aged testes**
884 **a,** Representative TUNEL staining in testis sections from young control (3-months), vitamin
885 E–deficient (VE(−)), aged (18-months) control and aged vitamin E–supplemented (VE(+))

886 mice; asterisks mark tubules containing TUNEL$^+$ cells. Scale bar: 200 µm. **b, c,** Quantification
887 of the percentage of tubules containing TUNEL$^+$ cells in young mice (control vs VE(−); **b**) and
888 aged mice (control vs VE(+); **c**). **d,** Representative images of CASP3$^+$/TUNEL$^+$ round
889 spermatids in young and aged testis sections. Scale bars: 50µm. Data are presented as mean ±
890 s.d. Significance was determined by two-tailed Student's *t*-test (**b, c**). Exact *P* values are given.
891 Sample size: $N = 6$ in each group. Each dot represents one mouse.
892
893 **Extended Data Fig. 6: Age-linked round spermatid loss skews Y/X output.**
894 Graphical summary of the model supported by this study, linking aging-associated lipid redox
895 stress to altered haploid sex-chromosome output. Along the male germline lineage, cell death
896 is enriched in pre-meiotic and meiotic stages, whereas post-meiotic round spermatids (RSs)
897 exhibit heightened lipid peroxidation and ferroptosis-like vulnerability. In young mice, lipid
898 peroxidation is low and X- and Y-bearing RSs are maintained, resulting in a balanced Y/X
899 output. In aged mice, lipid peroxidation is increased and RS loss is associated with a skewed
900 Y/X chromosome ratio. Vitamin E deficiency phenocopies the aging-associated increase in
901 lipid peroxidation and RS, whereas vitamin E supplementation reduces lipid peroxidation and
902 restores Y/X balance. Arrows denote the direction of change; the lightning symbol indicates
903 RS loss. Illustration was created in BioRender. Germeraad, J. (2026)
904 https://BioRender.com/k04h4kg

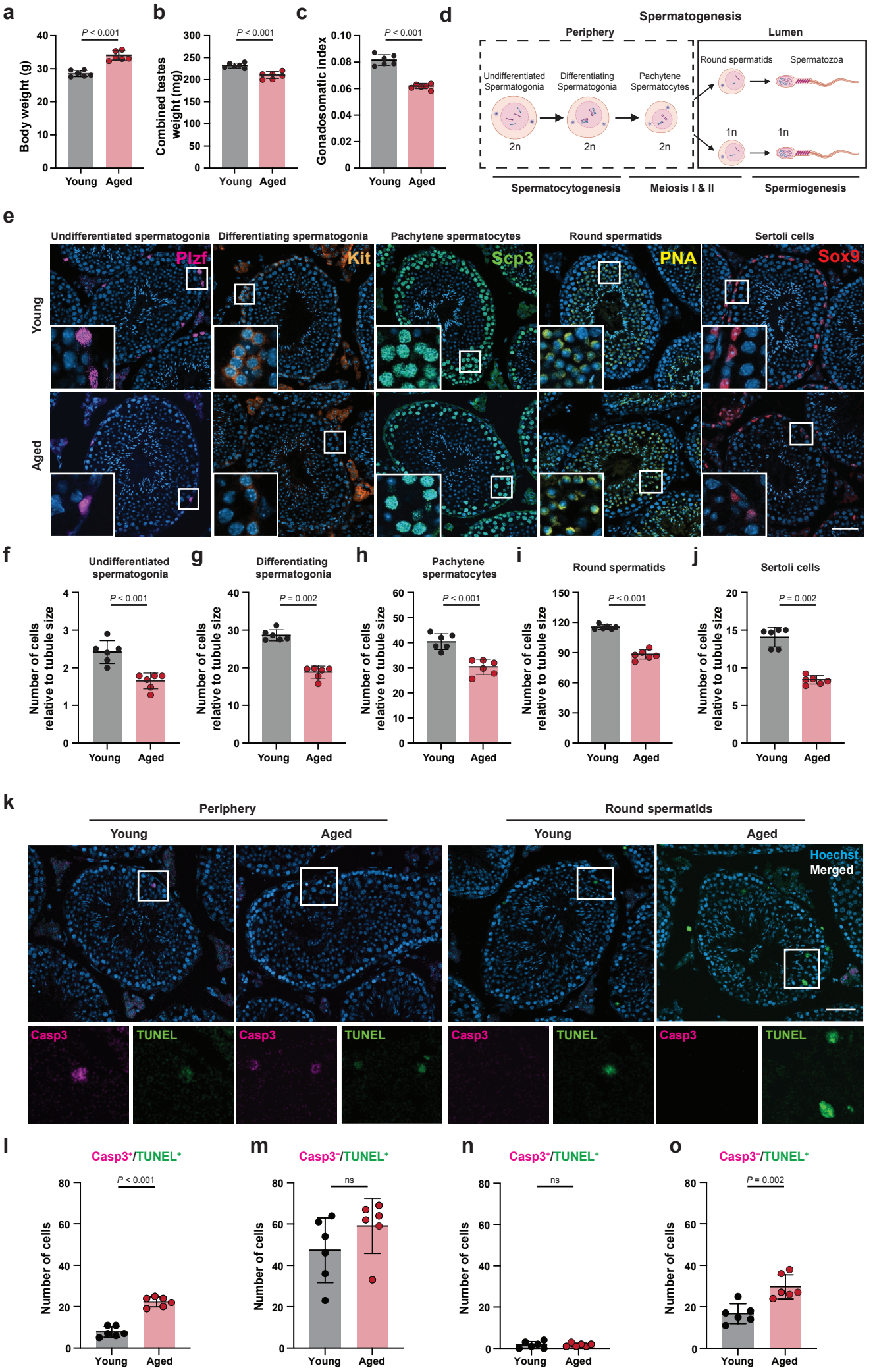
a
Body weight (g)
P < 0.001
Young
Aged
b
Combined testes weight (mg)
P < 0.001
c
Gonadosomatic index
P < 0.001
d
Spermatogenesis
Periphery
Lumen
Undifferentiated Spermatogonia
Differentiating Spermatogonia
Pachytene Spermatocytes
Round spermatids
Spermatozoa
2n
1n
Spermatocytogenesis
Meiosis I & II
Spermiogenesis
e
Undifferentiated spermatogonia
Differentiating spermatogonia
Pachytene spermatocytes
Round spermatids
Sertoli cells
Plzf
Kit
Scp3
PNA
Sox9
Young
Aged
f
Undifferentiated spermatogonia
g
Differentiating spermatogonia
h
Pachytene spermatocytes
i
Round spermatids
j
Sertoli cells
Number of cells relative to tubule size
P < 0.001
P = 0.002
k
Periphery
Round spermatids
Hoechst
Merged
Casp3
TUNEL
l
Casp3+/TUNEL+
m
Casp3−/TUNEL+
n
Casp3+/TUNEL+
o
Casp3−/TUNEL+
Number of cells
ns

Figure 1

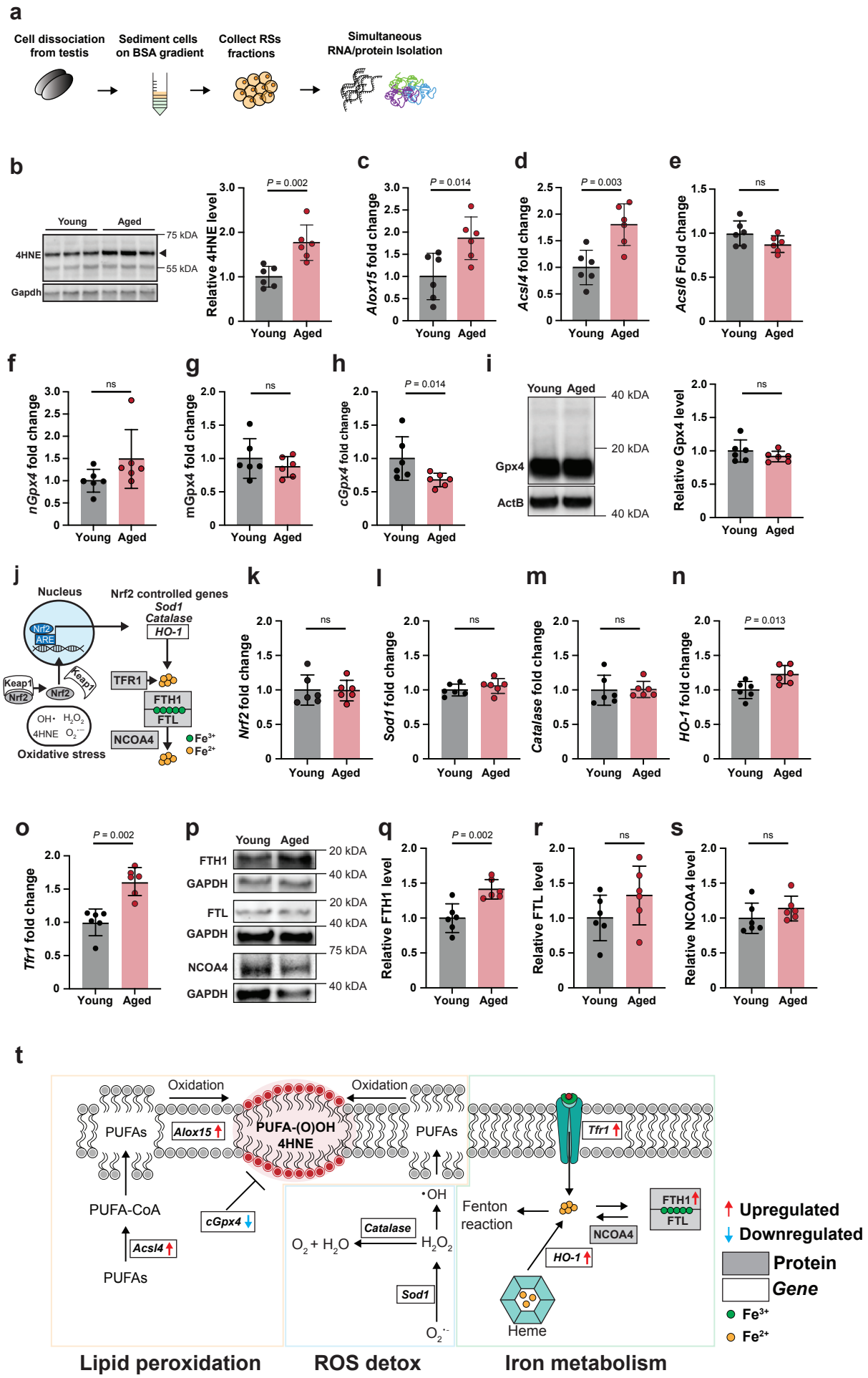
a
Cell dissociation from testis
Sediment cells on BSA gradient
Collect RSs fractions
Simultaneous RNA/protein Isolation
b
Young
Aged
4HNE
Gapdh
75 kDA
55 kDA
Relative 4HNE level
P = 0.002
c
Alox15 fold change
P = 0.014
d
Acsl4 fold change
P = 0.003
e
Acsl6 Fold change
ns
f
nGpx4 fold change
ns
g
mGpx4 fold change
ns
h
cGpx4 fold change
P = 0.014
i
Gpx4
ActB
40 kDA
20 kDA
Relative Gpx4 level
ns
j
Nucleus
Nrf2 controlled genes
Sod1
Catalase
HO-1
Nrf2
ARE
Keap1
TFR1
FTH1
FTL
NCOA4
Fe3+
Fe2+
Oxidative stress
k
Nrf2 fold change
ns
l
Sod1 fold change
ns
m
Catalase fold change
ns
n
HO-1 fold change
P = 0.013
o
Tfr1 fold change
P = 0.002
p
FTH1
GAPDH
FTL
NCOA4
20 kDA
40 kDA
75 kDA
q
Relative FTH1 level
P = 0.002
r
Relative FTL level
ns
s
Relative NCOA4 level
ns
t
Oxidation
PUFAs
Alox15
PUFA-(O)OH
4HNE
PUFA-CoA
Acsl4
cGpx4
Catalase
Sod1
Fenton reaction
Tfr1
FTH1
FTL
NCOA4
HO-1
Heme
Upregulated
Downregulated
Protein
Gene
Lipid peroxidation
ROS detox
Iron metabolism

Figure 2

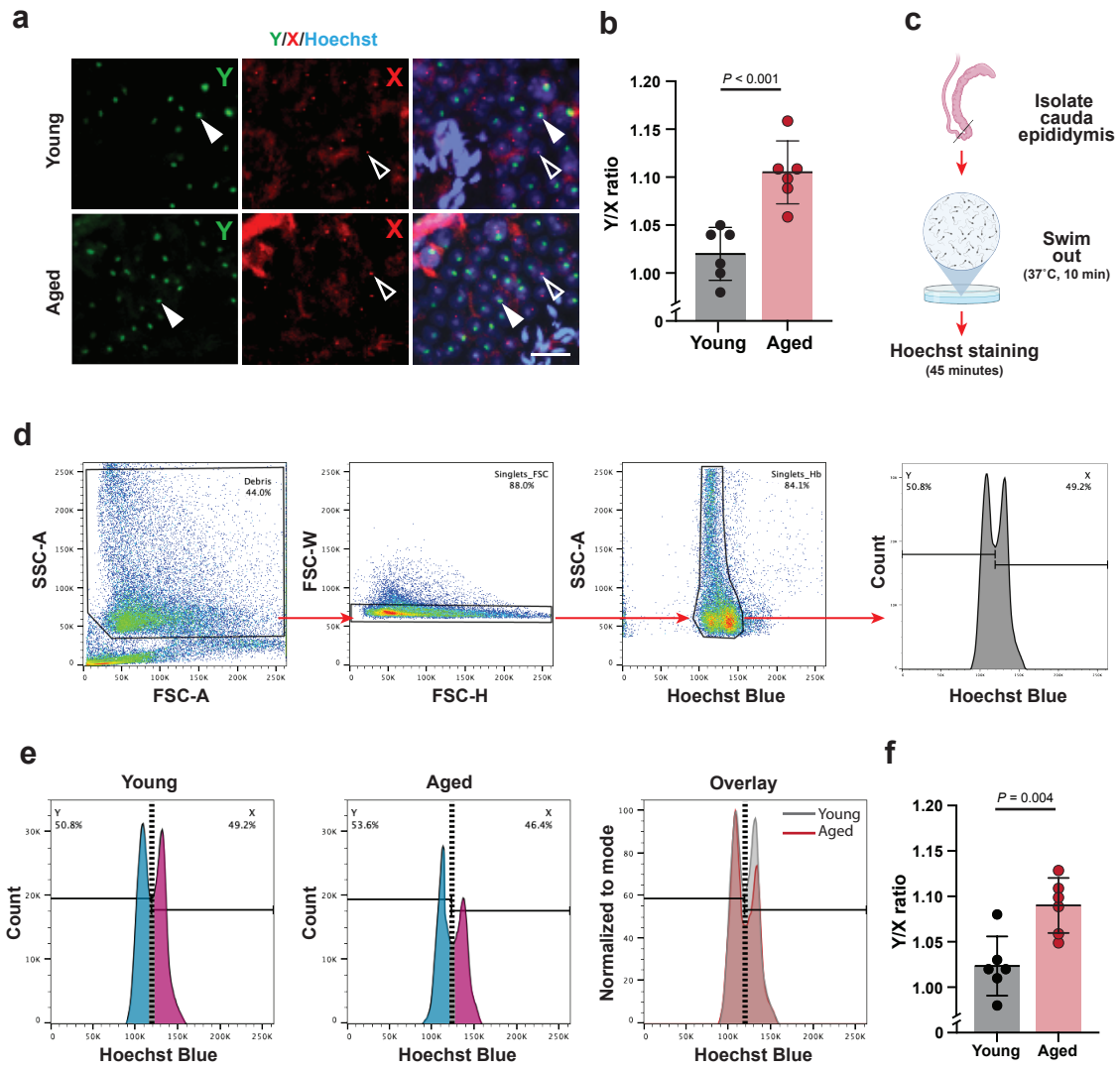
a
Y/X/Hoechst
Young
Aged
Y
X
b
P < 0.001
Y/X ratio
1.20
1.15
1.10
1.05
1.00
0
Young
Aged
c
Isolate cauda epididymis
Swim out
(37˚C, 10 min)
Hoechst staining
(45 minutes)
d
SSC-A
FSC-A
Debris 44.0%
FSC-W
FSC-H
Singlets_FSC 88.0%
SSC-A
Hoechst Blue
Singlets_Hb 84.1%
Count
Hoechst Blue
Y 50.8%
X 49.2%
e
Young
Aged
Overlay
Count
Hoechst Blue
Y 50.8%
X 49.2%
Y 53.6%
X 46.4%
Normalized to mode
Young
Aged
f
P = 0.004
Y/X ratio
Young
Aged

Figure 3

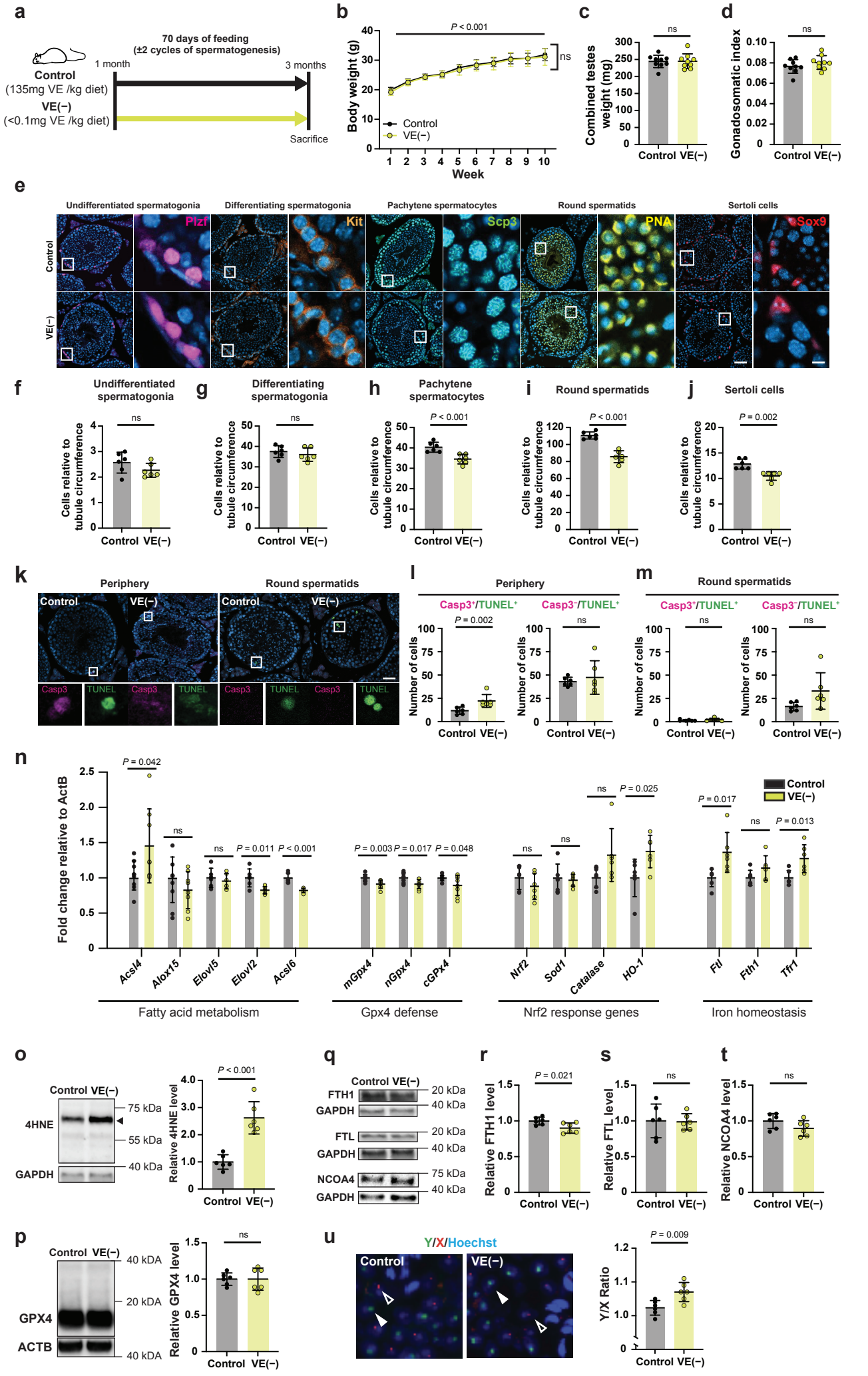
a
70 days of feeding
(±2 cycles of spermatogenesis)
1 month
3 months
Control
(135mg VE /kg diet)
VE(−)
(<0.1mg VE /kg diet)
Sacrifice
b
P < 0.001
ns
Body weight (g)
Control
VE(−)
Week
c
ns
Combined testes weight (mg)
Control VE(−)
d
ns
Gonadosomatic index
Control VE(−)
e
Undifferentiated spermatogonia
Differentiating spermatogonia
Pachytene spermatocytes
Round spermatids
Sertoli cells
Control
VE(−)
Plzf
Kit
Scp3
PNA
Sox9
f
Undifferentiated spermatogonia
g
Differentiating spermatogonia
h
Pachytene spermatocytes
i
Round spermatids
j
Sertoli cells
Cells relative to tubule circumference
P = 0.002
Control VE(−)
k
Periphery
Round spermatids
Control
VE(−)
Casp3
TUNEL
l
Periphery
Casp3+/TUNEL+
Casp3−/TUNEL+
P = 0.002
Number of cells
m
Round spermatids
n
Fold change relative to ActB
P = 0.042
P = 0.011
P < 0.001
P = 0.003
P = 0.017
P = 0.048
P = 0.025
P = 0.017
P = 0.013
Control
VE(−)
Acsl4
Alox15
Elovl5
Elovl2
Acsl6
mGpx4
nGpx4
cGPx4
Nrf2
Sod1
Catalase
HO-1
Ftl
Fth1
Tfr1
Fatty acid metabolism
Gpx4 defense
Nrf2 response genes
Iron homeostasis
o
Control VE(−)
4HNE
GAPDH
75 kDa
55 kDa
40 kDa
Relative 4HNE level
P < 0.001
q
Control VE(−)
FTH1
GAPDH
FTL
NCOA4
20 kDa
40 kDa
75 kDa
r
Relative FTH1 level
P = 0.021
s
Relative FTL level
t
Relative NCOA4 level
p
GPX4
ACTB
Relative GPX4 level
u
Y/X/Hoechst
Control
VE(−)
Y/X Ratio
P = 0.009

Figure 4

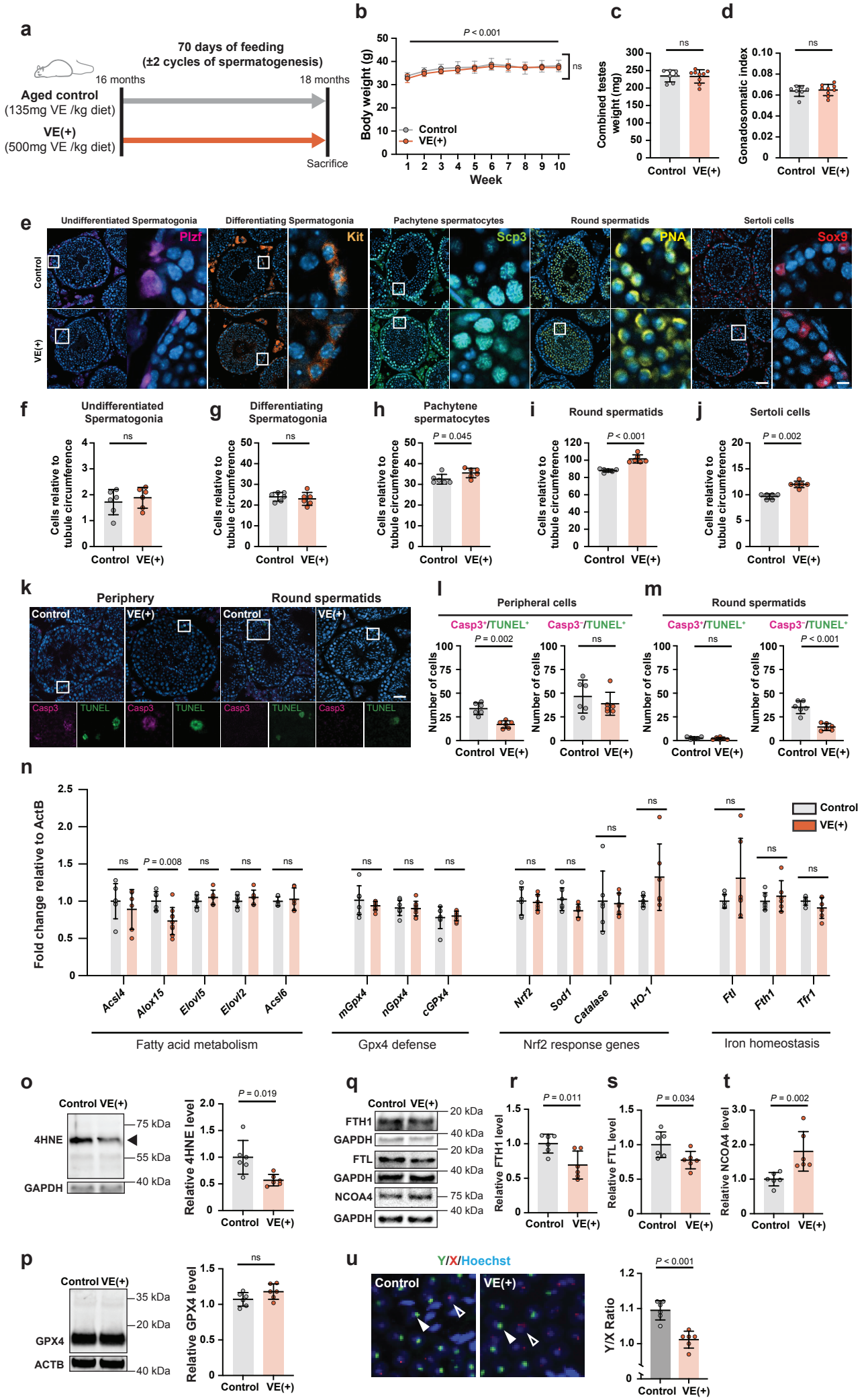
a
70 days of feeding
(±2 cycles of spermatogenesis)
16 months
18 months
Aged control
(135mg VE /kg diet)
VE(+)
(500mg VE /kg diet)
Sacrifice
b
P < 0.001
ns
Body weight (g)
Week
Control
VE(+)
c
Combined testes weight (mg)
d
Gonadosomatic index
e
Undifferentiated Spermatogonia
Differentiating Spermatogonia
Pachytene spermatocytes
Round spermatids
Sertoli cells
Plzf
Kit
Scp3
PNA
Sox9
Control
VE(+)
f
Undifferentiated Spermatogonia
g
Differentiating Spermatogonia
h
Pachytene spermatocytes
P = 0.045
i
Round spermatids
P < 0.001
j
Sertoli cells
P = 0.002
Cells relative to tubule circumference
k
Periphery
Round spermatids
Casp3
TUNEL
l
Peripheral cells
Casp3+/TUNEL+
Casp3−/TUNEL+
P = 0.002
Number of cells
m
Round spermatids
P < 0.001
n
Fold change relative to ActB
P = 0.008
Acsl4
Alox15
Elovl5
Elovl2
Acsl6
mGpx4
nGpx4
cGPx4
Nrf2
Sod1
Catalase
HO-1
Ftl
Fth1
Tfr1
Fatty acid metabolism
Gpx4 defense
Nrf2 response genes
Iron homeostasis
o
4HNE
GAPDH
75 kDa
55 kDa
40 kDa
P = 0.019
Relative 4HNE level
q
FTH1
FTL
NCOA4
20 kDa
40 kDa
75 kDa
r
P = 0.011
Relative FTH1 level
s
P = 0.034
Relative FTL level
t
P = 0.002
Relative NCOA4 level
p
GPX4
ACTB
35 kDa
20 kDa
Relative GPX4 level
u
Y/X/Hoechst
P < 0.001
Y/X Ratio

Figure 5

a

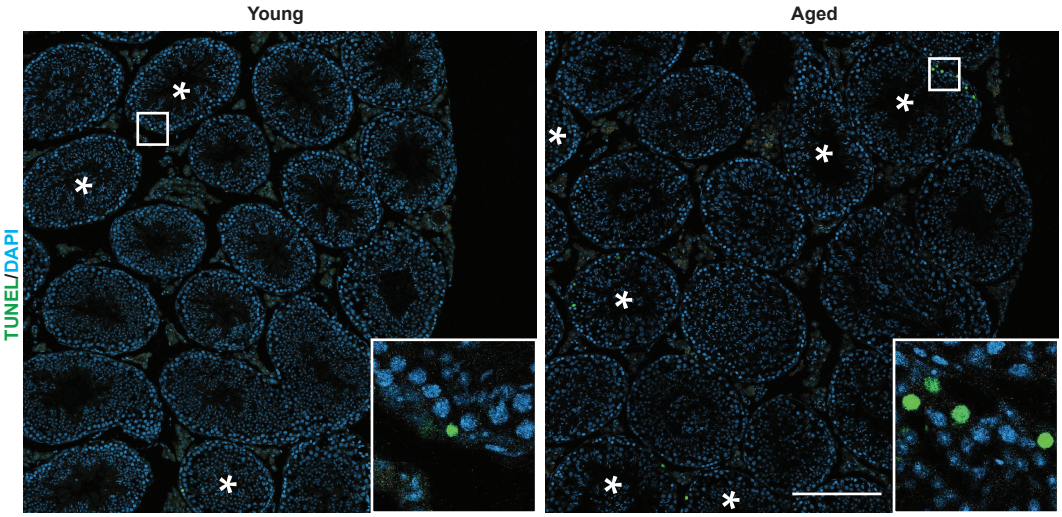

b

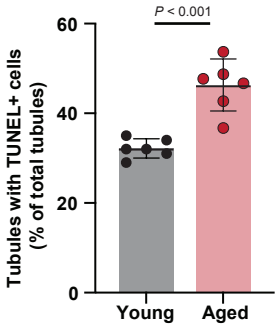

c

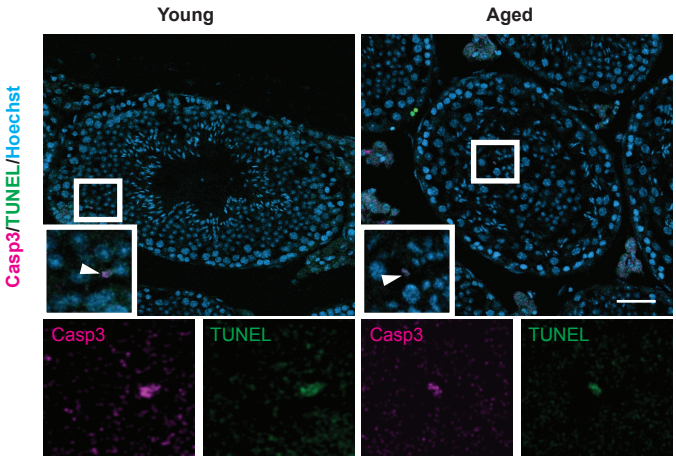

Extended data 1

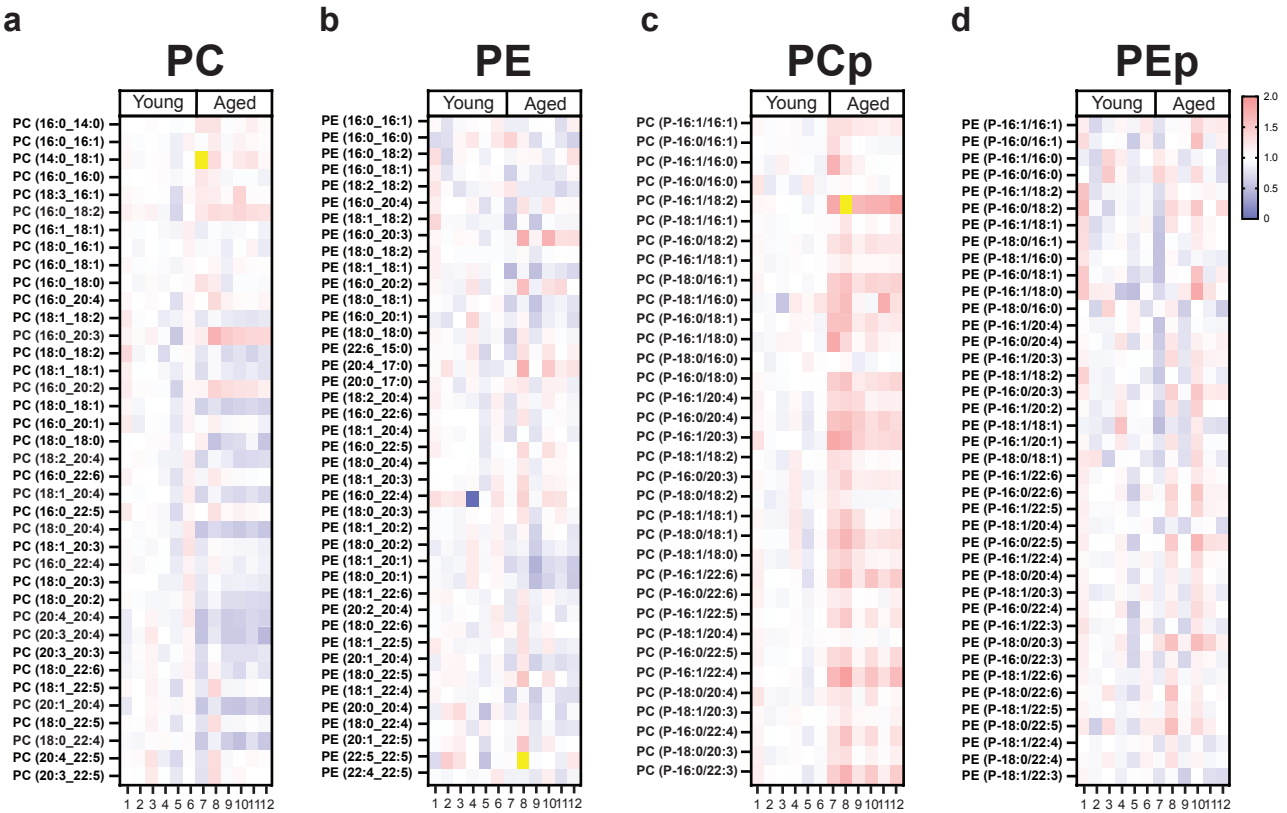

Extended data 2

a

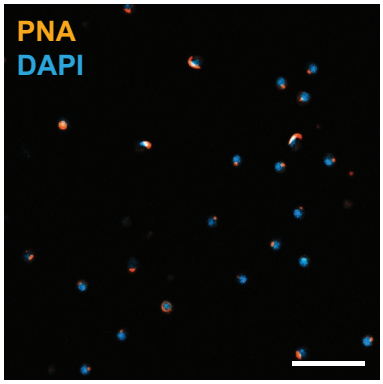

b

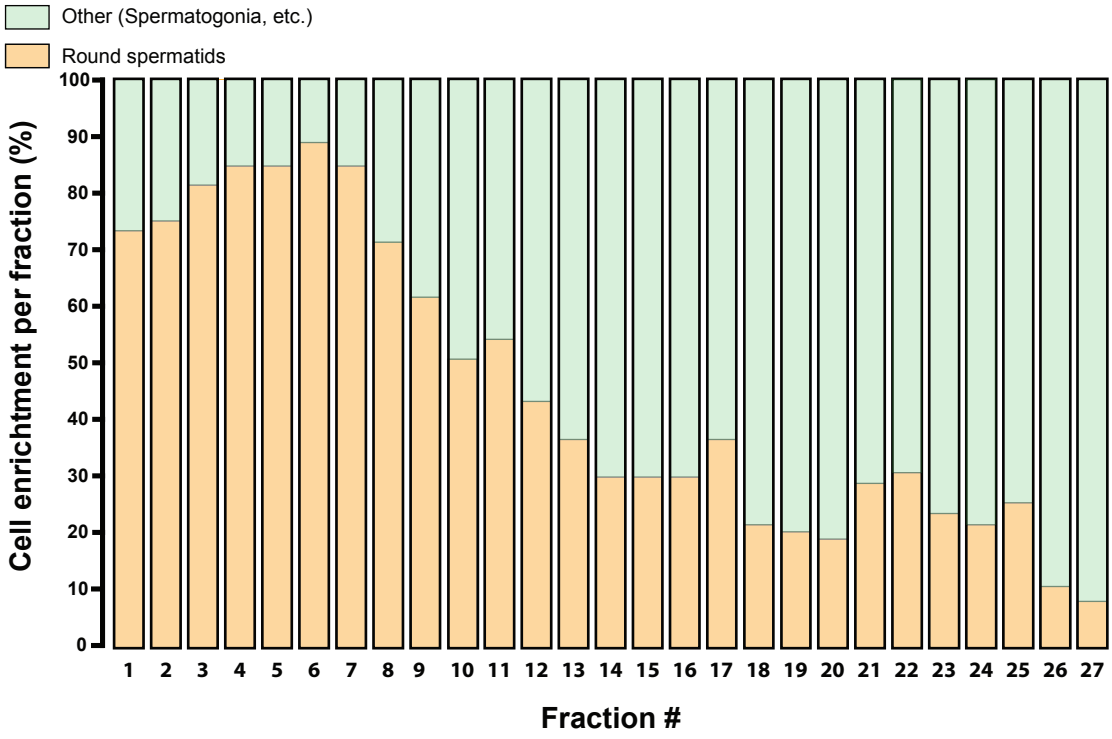

Extended data 3

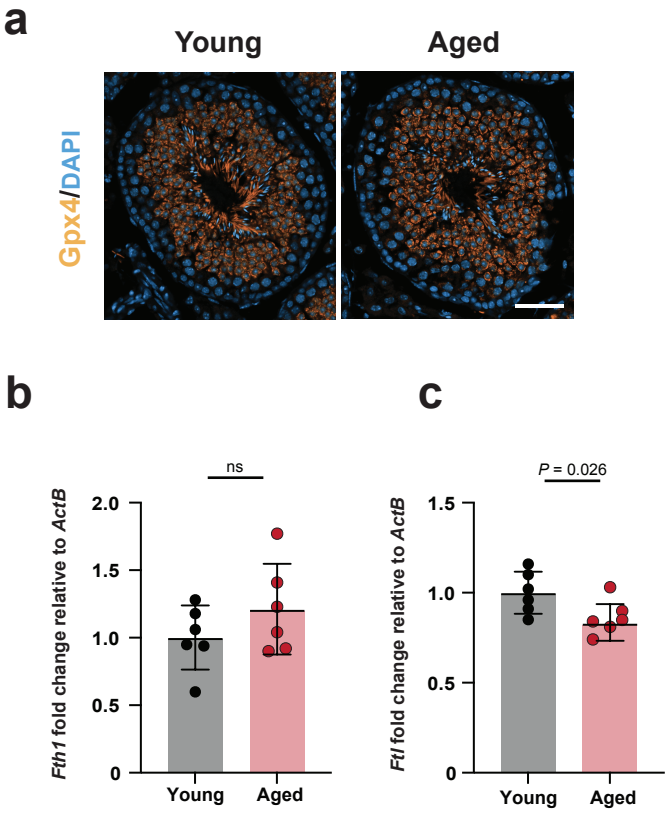

Extended data 4

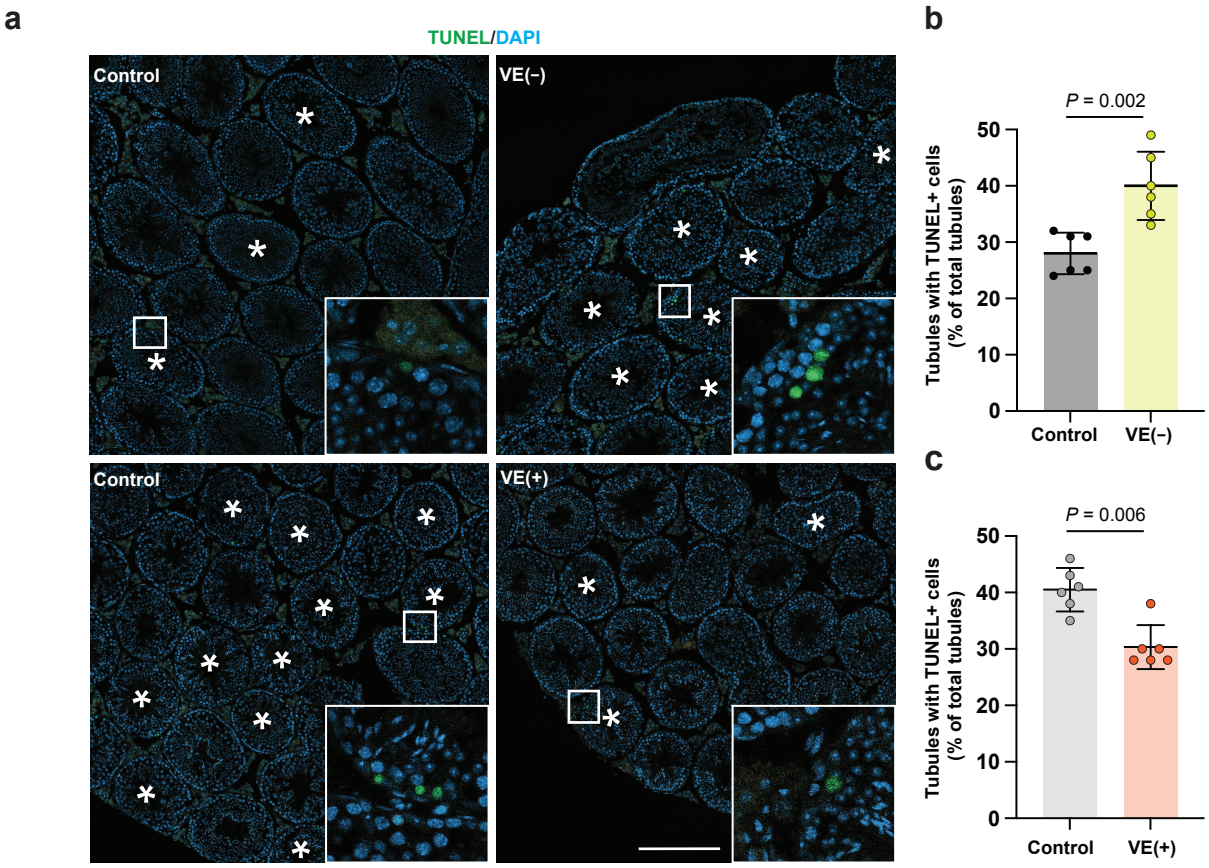

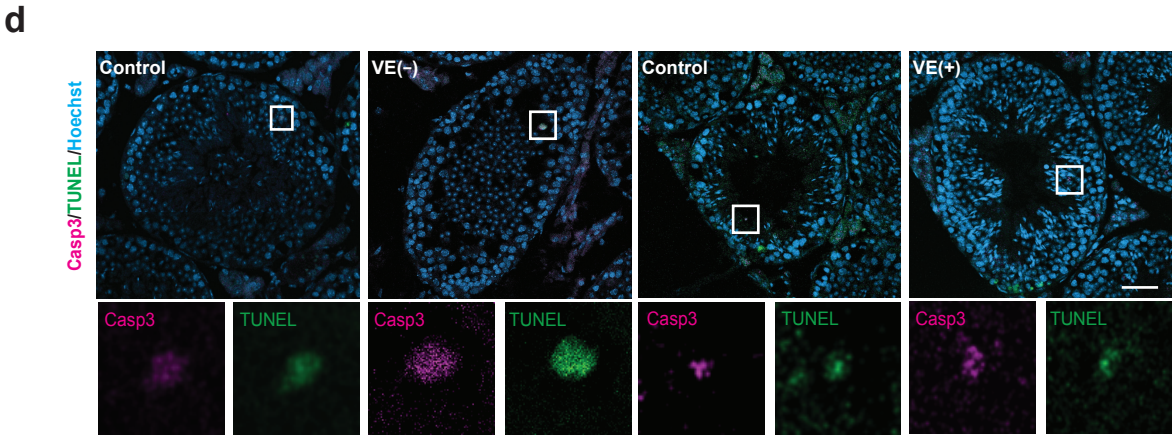

Extended data 5

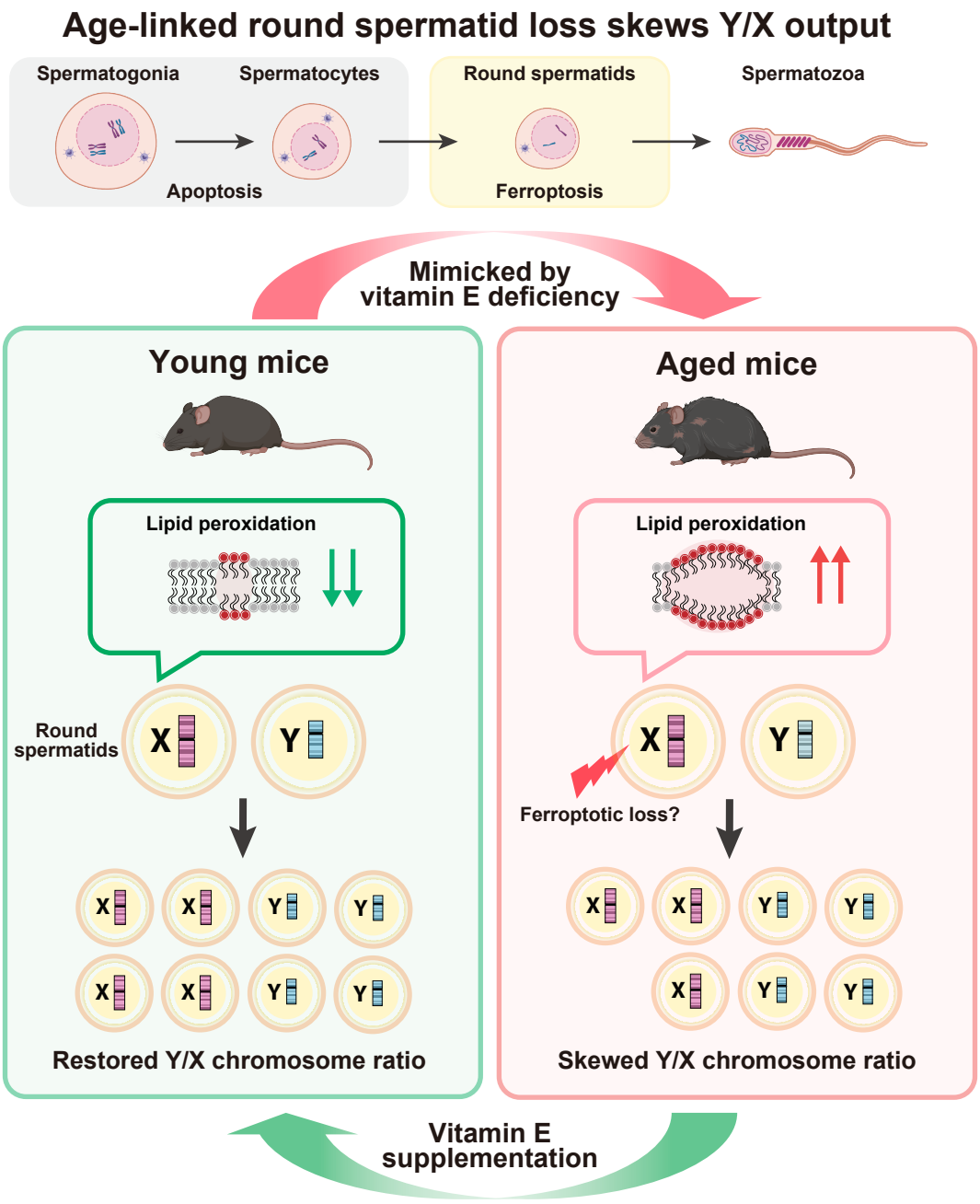

Extended data 6